

Canonical Variates in Wasserstein Metric Space

Jia Li

Department of Statistics, The Pennsylvania State University

Lin Lin

Department of Biostatistics and Bioinformatics, Duke University

Abstract

In this paper, we address the classification of instances represented by distributions on a vector space rather than single points. We consider classification algorithms based on pairwise distances, specifically, the Wasserstein metric between distributions. Central to our investigation is dimension reduction within the Wasserstein metric space to enhance classification accuracy. We introduce a novel approach grounded in the principle of maximizing Fisher’s ratio, defined as the quotient of between-class variation to within-class variation. The directions in which this ratio is maximized are termed discriminant coordinates or canonical variates axes. In practice, both between-class and within-class variations are defined as the average squared Wasserstein distances between pairs of distributions, with the pairs either belonging to the same class or to different classes. This ratio optimization is achieved through an iterative algorithm, which alternates between optimal transport and maximization steps within the vector space. Empirical studies are conducted to assess the algorithm’s convergence; and experimental results demonstrate that the dimension reduction technique substantially enhances classification performance. Moreover, the new method outperforms well-established algorithms that operate on vector representations derived from distributional data. It also exhibits robustness to variations in how instances are summarized by distributions, such as the number of components in a Gaussian mixture model (GMM) representation.

Keywords: Optimal transport, Wasserstein distance, Canonical coordinates, Dimension reduction, Distributional data

1 Introduction

In numerous biomedical contexts, a common challenge is the classification of subjects, each represented not by a single feature vector but by a sample of measurements forming an

empirical distribution, referred to here as a *data cloud*. A prime example is cellular-based immunoprofiling, where each subject is represented by measurements of many individual cells collected under different conditions such as disease, therapeutic intervention, or vaccination. This includes applications such as cancer immunotherapy, infectious disease monitoring, and HIV vaccine research, where distinguishing protective from non-protective immune signatures is of particular interest. Widely used single-cell technologies, including flow cytometry, mass cytometry (CyTOF), and single-cell RNA sequencing (scRNA-seq), enable the measurement of cellular constituents from an individual’s sample (often blood) (Furman et al., 2013; Lin et al., 2015; Lingblom et al., 2018; Aleman et al., 2021; Stefanski et al., 2022; Zhang et al., 2023a; Rubio et al., 2023; Aid et al., 2023; Zhang et al., 2025; Sun et al., 2025). The resulting single-cell data are typically organized as a matrix, where each row corresponds to a cell and each column to a measured marker (such as a protein or gene). This matrix serves as the fundamental representation of an individual’s profile and is used to predict clinical outcomes or disease status. Unlike traditional vector or tabular data, however, each instance here is itself a matrix—each row a distinct point (cell) in a high-dimensional data cloud. It is therefore important to distinguish a standard matrix from a *data-cloud matrix*: in the latter, the order of rows carries no information. Randomly permuting the rows does not alter the underlying characteristics of the instance.

In this paper, a data cloud can be taken directly as a distribution, in which the observed data points are regarded as *support points* of a uniform distribution. By allowing unequal weights on these support points, the same framework naturally extends to non-uniform distributions. We further model continuous distributions by the Gaussian Mixture Model (GMM), a widely used and highly representative family of distributions.

There are two principal schools of thought in the classification of data clouds: (1) vector representation approaches and (2) distributional representation approaches. In the first school, data clouds are transformed into feature vectors, often by partitioning the data into clusters. When clusters generated across different instances can be assigned coherent labels, attributes such as the proportion of points in each cluster or the mean values within clusters can be aggregated into a feature vector, enabling the use of a broad range of machine learning algorithms. Achieving coherent labeling, however, often requires supplementary domain knowledge or manual inspection, and challenges arise when algorithm-derived clusters fail to align naturally across datasets (Cron et al., 2013; Johansen and Quon, 2019; Zhang et al., 2020; Li and Lin, 2021; Zhang et al., 2023b; Cui et al., 2024). In single-cell analysis, this strategy is exemplified by first identifying cell subsets through clustering or manual gating (Brummelman et al., 2019). Summary statistics of these subsets, such as cell-type proportions or mean marker expression levels, are then compiled into feature vectors for outcome prediction (Gray et al., 2019; Lin et al., 2015; Seshadri et al., 2015; Shah et al., 2017; Zou et al., 2023; Ager et al., 2023; Mettu et al., 2023; Dyikanov et al., 2024; Anwar et al., 2025). While convenient, this practice often discards essential distributional characteristics, e.g., multimodality, skewness, or variance, that may carry critical biological information. In contrast, the second school models data clouds directly as probability distributions and compares them using classification algorithms designed for distributional data. Because such data lack algebraic structure at the instance level, these methods typically rely on distance-based classification, with the Wasserstein distance being one of the

most widely adopted measures (Nguyen et al., 2019; Yi and Stanley, 2022; Huizing et al., 2022; Joodaki et al., 2024; Wang et al., 2025).

We focus on the second school of approaches: classification of distributional data. Our objective is to develop a principled framework for dimensionality reduction in distance-based classification, with particular emphasis on the Wasserstein metric. As detailed in the following sections, we formulate this task as the maximization of Fisher’s ratio within the Wasserstein metric space. Because variance is inherently linked to the sum of all pairwise Euclidean distances, Fisher’s ratio can be equivalently expressed using pairwise distances. We adopt this pairwise formulation and further propose a scheme that emphasizes distances between instances that are potentially difficult to classify. Prioritizing such “difficult” pairs often leads to improved classification performance after dimensionality reduction.

To effectively handle continuous distributions, we adopt GMMs as a flexible representation and replace the Wasserstein metric with the *Minimized Aggregated Wasserstein* (MAW) distance (Chen et al., 2019), which enables more efficient optimization. Importantly, discrete distribution with finite support can be viewed as special cases of GMMs with singular covariance matrices (i.e., zero variances in all dimensions), in which case the MAW distance reduces to the standard Wasserstein distance. As a result, our framework applies seamlessly to both discrete and continuous settings. More broadly, since continuous distributions are commonly approximated either through discretization (sampling) or through GMM modeling, our method is compatible with both strategies.

It is worthwhile to note an interesting method called Wasserstein discriminant analysis (WDA) by Flamary et al. (2018) for data in the Euclidean space. Although our work also involves the Wasserstein distance, the research problem addressed here is intrinsically different than that of WDA. In Flamary et al. (2018), a new criterion is developed for discriminant analysis on data points in the Euclidean space; and the Wasserstein metric is used to measure the distance between class-level distributions. In contrast, our work aims at dimension reduction for data instances that are themselves distributions. At the class level, instead of using the Wasserstein distance directly, we employ a simple summation of pairwise distances, as has been adopted in Fisher’s ratio or other related criteria. Therefore, our novelty lies not in defining a new discriminant criterion for vector data, but in addressing the challenges inherent in analyzing distributional data, both discrete and continuous.

Other related works have aimed to reduce the computational cost of the Wasserstein distance. For instance, the sliced-Wasserstein distance (Bonneel et al., 2015; Tanguy et al., 2023) has been proposed based on linear slicing of probability distributions. Further extensions, such as the max-sliced-Wasserstein (Deshpande et al., 2019; Paty and Cuturi, 2019) and generalized sliced-Wasserstein (Kolouri et al., 2019), have also been explored. Although these methods search for linear projections or subspaces to compute the distance, their objectives differ from our goal of maximizing Fisher’s ratio. Another extension of the Wasserstein distance, the Gromov-Wasserstein distance (Mémoli, 2011; Delon et al., 2022), generalizes the framework to compare distributions supported on different metric spaces.

The remainder of the paper is organized as follows. Section 2 reviews the Wasserstein metric, its connection to optimal transport (Villani, 2003), and the MAW distance. Section 3 details the formulation of the dimension reduction problem and the corresponding

optimization algorithm. Experimental results are provided in Section 4. We conclude in Section 5.

2 Preliminaries

Consider two probability distributions (discrete or continuous) \mathcal{P}_i , $i = 1, 2$, on the d -dimensional Euclidean space \mathbb{R}^d . For clarity of presentation, suppose that random vectors X_i follow distribution \mathcal{P}_i , $i = 1, 2$. A coupling between \mathcal{P}_1 and \mathcal{P}_2 is defined as a joint distribution of (X_1, X_2) whose marginals are fixed at \mathcal{P}_1 and \mathcal{P}_2 , respectively. Denote the set of all such couplings by Π , with a particular coupling written as π . When necessary, we stress the dependence of Π on the marginal constraints by writing $\Pi_{\mathcal{P}_1, \mathcal{P}_2}$, or more simply Π_{k_1, k_2} when \mathcal{P}_{k_1} and \mathcal{P}_{k_2} are under discussion. The L_p ($p \geq 1$) Wasserstein metric between \mathcal{P}_1 and \mathcal{P}_2 is defined as

$$W^p(\mathcal{P}_1, \mathcal{P}_2) := \min_{\pi \in \Pi} E_{\pi} \|X_1 - X_2\|^p.$$

In this work, we adopt the L_2 norm Wasserstein distance, the most commonly used case.

Let $\mathcal{Q}_k = \{(p_j^{(k)}, x_j^{(k)}), j = 1, \dots, m_k\}$, $k = 1, \dots, n$, denote a discrete distribution, where m_k is the number of support points, $p_j^{(k)}$ is the probability assigned to support point $x_j^{(k)} \in \mathbb{R}^d$, and $\sum_j p_j^{(k)} = 1$. A coupling π is then characterized by joint probabilities $\pi_{i,j}$ assigned to the Cartesian product $(x_i^{(k_1)}, x_j^{(k_2)})$, subject to the marginal constraints $\sum_{j=1}^{m_{k_2}} \pi_{i,j} = p_i^{(k_1)}$, $i = 1, \dots, k_1$ and $\sum_{i=1}^{m_{k_1}} \pi_{i,j} = p_j^{(k_2)}$, $j = 1, \dots, k_2$. Let Π_{k_1, k_2} denote the set of all couplings for \mathcal{Q}_{k_1} and \mathcal{Q}_{k_2} . The L_2 Wasserstein distance is then

$$W^2(\mathcal{Q}_{k_1}, \mathcal{Q}_{k_2}) = \min_{\pi \in \Pi_{k_1, k_2}} \sum_{i=1}^{m_{k_1}} \sum_{j=1}^{m_{k_2}} \pi_{i,j} \|x_i^{(k_1)} - x_j^{(k_2)}\|^2. \quad (1)$$

From the perspective of optimization, this formulation is precisely the classical optimal transport (OT) problem (Villani, 2003).

For continuous distributions, closed-form expressions for the Wasserstein distance are generally unavailable, except in special cases such as Gaussian distributions. A common strategy is to approximate continuous distributions with empirical discrete distributions derived from samples. However, this approach is severely limited by the curse of dimensionality (Pele and Werman, 2009; Cuturi, 2013; Wang et al., 2023). To address this, Chen et al. (2019) introduced the Minimized Aggregated Wasserstein (MAW) distance, which models a continuous distribution using a GMM.

Consider two Gaussian distributions ϕ_1 and ϕ_2 in \mathbb{R}^d , parameterized by (μ_i, Σ_i) , $i = 1, 2$, where μ_i is the mean vector and Σ_i is the covariance matrix. Suppose $Z_1 \sim \phi_1$ and $Z_2 \sim \phi_2$. Let Π_{ϕ_1, ϕ_2} be the set of couplings of (Z_1, Z_2) with fixed marginals ϕ_1 and ϕ_2 . Then the squared Wasserstein distance $W^2(\phi_1, \phi_2)$ is given by the closed formula:

$$W^2(\phi_1, \phi_2) = \|\mu_1 - \mu_2\|^2 + \text{tr} \left[\Sigma_1 + \Sigma_2 - 2 \left(\Sigma_1^{\frac{1}{2}} \Sigma_2 \Sigma_1^{\frac{1}{2}} \right)^{\frac{1}{2}} \right]. \quad (2)$$

Now consider GMMs $\mathcal{G}_k = \{(p_i^{(k)}, \phi_i^{(k)}), i = 1, \dots, m_k\}$, $k = 1, \dots, n$, where m_k is the number of Gaussian components and $p_i^{(k)}$ is the prior weight of component $\phi_i^{(k)}$. Similar to the discrete case, let Π_{k_1, k_2} be the set of couplings between the priors of \mathcal{G}_{k_1} and \mathcal{G}_{k_2} . The MAW distance between \mathcal{G}_{k_1} and \mathcal{G}_{k_2} is defined as

$$\widetilde{W}^2(\mathcal{G}_{k_1}, \mathcal{G}_{k_2}) = \min_{\pi \in \Pi_{k_1, k_2}} \sum_{i=1}^{m_{k_1}} \sum_{j=1}^{m_{k_2}} \pi_{i,j} W^2(\phi_i^{(k_1)}, \phi_j^{(k_2)}).$$

Under the MAW framework, a GMM is treated as a discrete distribution over Gaussian components, and the Wasserstein distance between these components is the counterpart of the Euclidean distance between support points in discrete distributions. The availability of a closed-form solution for the Wasserstein distance between Gaussian distributions has motivated the definition of MAW, which is also solved by OT. Delon and Desolneux (2020) derived theoretical properties of MAW; and more recently, Delon et al. (2023) applied this distance to texture synthesis. In practice, this distance obviates the need for generating large samples from high-dimensional spaces. Lin et al. (2023) presents an application demonstrating this advantage. Furthermore, even in scenarios with high-dimensional data, the required number of components to accurately model data is often low, ensuring that the computation of MAW remains efficient.

Finally, we compare the Wasserstein distance for discrete distributions with MAW for GMMs. Note that when covariance matrices are zero, the Wasserstein distance between two Gaussian components reduces to the Euclidean distance between their means. Hence, a discrete distribution can be viewed as a special case of a GMM with zero covariances, and MAW as a natural generalization of the Wasserstein distance between discrete distributions. The only additional computation lies in the second term of Eq. (2). Importantly, MAW was designed to approximate the Wasserstein distance between continuous distributions, rather than between discrete ones. As discussed earlier, discretization is another approximation strategy, but it suffers severely from the curse of dimensionality.

3 Algorithm

3.1 Optimization criterion

For clarity, we first present the proposed principle of dimension reduction in the context of discrete distributions. The same principle extends naturally to GMMs, with $W^2(\mathcal{Q}_{k_1}, \mathcal{Q}_{k_2})$ replaced by $\widetilde{W}^2(\mathcal{G}_{k_1}, \mathcal{G}_{k_2})$.

Denote the class label associated with \mathcal{Q}_k by Y_k , $Y_k \in \mathcal{Y}$, $\mathcal{Y} = \{1, \dots, M\}$, where M is the number of classes. Let $a_i = (a_{1,i}, a_{2,i}, \dots, a_{d,i})^t \in \mathbb{R}^d$ be a projection direction (not normalized). Let $A = (a_1, a_2, \dots, a_{d'})$ be a matrix of dimension $d \times d'$, where $d' < d$. The linear transform to reduce the dimension of $x \in \mathbb{R}^d$ to d' is $A^t \cdot x$. We call the distribution induced by the projection of the support points to the lower dimension the *projected distribution* and denote it by $P(\mathcal{Q}_k, A) = \{(p_j^{(k)}, A^t \cdot x_j^{(k)}), j = 1, \dots, m_k\}$. With a slight abuse of notation, for vector $a \in \mathbb{R}^d$, $P(\mathcal{Q}_k, a) = \{(p_j^{(k)}, a^t \cdot x_j^{(k)}), j = 1, \dots, m_k\}$.

Let set \mathcal{I}_B contain pairs of indices (k_1, k_2) such that the k_1 th and k_2 th instances have different classes, that is, $Y_{k_1} \neq Y_{k_2}$. Let \mathcal{I}_W contain pairs of indices belonging to the same class. As will be discussed later, \mathcal{I}_B (or \mathcal{I}_W) may not contain all the pairs of instances with different classes (or all the pairs within the same class). Define the average between-class variation by

$$\bar{V}_B(A) = \frac{1}{|\mathcal{I}_B|} \cdot \sum_{(k_1, k_2) \in \mathcal{I}_B} W^2(P(\mathcal{Q}_{k_1}, A), P(\mathcal{Q}_{k_2}, A)), \quad (3)$$

and the within-class variation by

$$\bar{V}_W(A) = \frac{1}{|\mathcal{I}_W|} \cdot \sum_{(k_1, k_2) \in \mathcal{I}_W} W^2(P(\mathcal{Q}_{k_1}, A), P(\mathcal{Q}_{k_2}, A)). \quad (4)$$

Finally, define *Fisher's ratio of variations*:

$$r(A) = \frac{\bar{V}_B(A)}{\bar{V}_W(A)}. \quad (5)$$

Again, with a slight abuse of notation, if we consider projection on one direction $a \in \mathbb{R}^d$, we use notations $\bar{V}_B(a)$, $\bar{V}_W(a)$, and $r(a)$.

The *Fisher's optimization criterion* to find an optimal projection direction is to maximize Fisher's ratio $r(a)$:

$$r(a^*) = \arg \max_a r(a). \quad (6)$$

We provide a few remarks on the Fisher's ratio and Fisher's optimization criterion. First, the concepts of Fisher's ratio and Fisher's optimization criterion were originally formulated in the context of linear discriminant analysis (LDA) (Hastie et al., 2009). We utilize these terms in our work, as the underlying principle remains consistent, namely, the maximization of the ratio between between-class and within-class variation. Within the realm of LDA, Fisher's ratio is also referred to as the *Rayleigh-Ritz quotient*.

Second, in the classical definition of Fisher's ratio, the between-class variation is determined by the variance of the projected mean vectors for each class, with weighting according to class proportions. Similarly, the within-class variation is defined as the weighted average of variances for each projected class. In the computation of these variances within the framework of LDA, per-class means are calculated as the arithmetic means of vectors. On the other hand, it can be shown that in the Euclidean space, the sample variance can be computed from the sample mean of pairwise squared distances, the two differing only by a constant factor. However, in the Wasserstein metric space, the equivalent of the arithmetic mean is the Wasserstein barycenter, whose computation is notably more demanding. By adopting the definition of Fisher's ratio based on pairwise distances, we avoid the need of computing barycenters. Nevertheless, efficient algorithms for computing Wasserstein barycenters have been developed by Benamou et al. (2015); Ye et al. (2017); Yang et al. (2021). A key rationale for using pairwise distances is that this approach provides the

flexibility of selecting pairwise distances for computing Fisher’s ratio. Empirical evidence suggests that prioritizing pairs more likely to contribute to classification errors often leads to enhancements in classification accuracy.

Finally, in the framework of LDA, the maximization of Fisher’s ratio is achieved through eigenvalue decomposition, as detailed in Hastie et al. (2009). However, the optimization problem as outlined in Eq. (6) presents unique challenges when applied to the Wasserstein distance. This complexity arises because the Wasserstein distance cannot be computed using a closed-form expression; instead, it necessitates numerical optimization. To address this, our primary strategy involves partitioning the variables involved in the optimization process into two distinct groups: the coupling weights used in calculating the Wasserstein distances, and the projection direction vector a . We then iteratively update these groups of variables in an alternating fashion.

We propose an iterative algorithm, referred to as *Optimal Transport And Fisher’s optimization* (OTAF), to solve the optimal projection direction a^* . The algorithm essentially performs coordinate descent along two groups of variables: the coupling weights versus the project direction. We explain the rationale of the algorithm before presenting it formally.

We first address discrete distributions, followed by GMMs. Both cases involve transforming Fisher’s ratio into a Rayleigh-Ritz quotient. This conversion is simpler for discrete distributions but requires an approximation for GMMs. Although the former can be viewed algorithmically as a special case of the latter, conceptually they are distinct. Hence, we discuss the derivation of the Rayleigh-Ritz quotient in the two cases separately but, for conciseness, explain its maximization only in the context of GMMs.

3.2 Discrete distributions

Suppose the optimal couplings between \mathcal{Q}_k ’s, $\pi^{(k_1, k_2)}$, $(k_1, k_2) \in \mathcal{I}_B \cup \mathcal{I}_W$, have been solved, that is, $\pi^{(k_1, k_2)} \in \Pi_{k_1, k_2}$ is a byproduct of solving Eq. (1). Define $\Pi^* := \{\pi^{(k_1, k_2)}, (k_1, k_2) \in \mathcal{I}_B \cup \mathcal{I}_W\}$. This is not the set of all couplings for a single pair, but one coupling per indexed pair in $\mathcal{I}_B \cup \mathcal{I}_W$. During OTAF, the coupling set Π^* is re-estimated at each iteration as the projection directions are updated. Initially, Π^* is constructed from the original data (before dimension reduction). The between-class and within-class variations become

$$\bar{V}_B(A, \Pi^*) = \frac{1}{|\mathcal{I}_B|} \sum_{(k_1, k_2) \in \mathcal{I}_B} \sum_{i=1}^{m_{k_1}} \sum_{j=1}^{m_{k_2}} \pi_{i,j}^{(k_1, k_2)} \cdot \left\| A^t \cdot x_i^{(k_1)} - A^t \cdot x_j^{(k_2)} \right\|^2,$$

$$\bar{V}_W(A, \Pi^*) = \frac{1}{|\mathcal{I}_W|} \sum_{(k_1, k_2) \in \mathcal{I}_W} \sum_{i=1}^{m_{k_1}} \sum_{j=1}^{m_{k_2}} \pi_{i,j}^{(k_1, k_2)} \cdot \left\| A^t \cdot x_i^{(k_1)} - A^t \cdot x_j^{(k_2)} \right\|^2.$$

To stress the fact that the couplings in Π^* are assumed given, we use the notations $\bar{V}_B(A, \Pi^*)$ and $\bar{V}_W(A, \Pi^*)$. Let matrices C_B and C_W (of dimension $d \times d$) be

$$C_B = \frac{1}{|\mathcal{I}_B|} \sum_{(k_1, k_2) \in \mathcal{I}_B} \sum_{i=1}^{m_{k_1}} \sum_{j=1}^{m_{k_2}} \pi_{i,j}^{(k_1, k_2)} \cdot \left(x_i^{(k_1)} - x_j^{(k_2)} \right) \cdot \left(x_i^{(k_1)} - x_j^{(k_2)} \right)^t, \quad (7)$$

$$C_W = \frac{1}{|\mathcal{I}_W|} \sum_{(k_1, k_2) \in \mathcal{I}_W} \sum_{i=1}^{m_{k_1}} \sum_{j=1}^{m_{k_2}} \pi_{i,j}^{(k_1, k_2)} \cdot \left(x_i^{(k_1)} - x_j^{(k_2)} \right) \cdot \left(x_i^{(k_1)} - x_j^{(k_2)} \right)^t. \quad (8)$$

The between-class variation $\bar{V}_B(A, \Pi^*)$ and the within-class variation $\bar{V}_W(A, \Pi^*)$ can be computed by

$$\bar{V}_B(A, \Pi^*) = \text{tr}(A^t C_B A) \quad (9)$$

$$\bar{V}_W(A, \Pi^*) = \text{tr}(A^t C_W A). \quad (10)$$

The derivation of these two equations is provided in Appendix A. In particular, if we optimize one projection direction a , $\text{tr}(a^t C_W a) = a^t C_W a$ and $\text{tr}(a^t C_B a) = a^t C_B a$. The Fisher's ratio becomes

$$r(a, \Pi^*) = \frac{a^t C_B a}{a^t C_W a}. \quad (11)$$

A sufficient condition under which OTAF yields a nondecreasing objective $r(a, \Pi^*)$ is presented in Theorem 1 (Section 3.4).

3.3 Gaussian mixture models

For GMMs, we again define the Fisher's ratio using Eq. (5), but $\bar{V}_B(A)$ and $\bar{V}_W(A)$ are computed using the MAW distance (denoted by \tilde{W}). Given a set of couplings between the Gaussian components of the indexed GMM pairs in $\mathcal{I}_B \cup \mathcal{I}_W$, denoted $\Pi^* := \{\boldsymbol{\pi}^{(k_1, k_2)}, (k_1, k_2) \in \mathcal{I}_B \cup \mathcal{I}_W\}$, the between-class and within-class variations $\bar{V}_B(A)$ and $\bar{V}_W(A)$ become, respectively:

$$\bar{V}_B(A, \Pi^*) = \frac{1}{|\mathcal{I}_B|} \sum_{(k_1, k_2) \in \mathcal{I}_B} \sum_{i=1}^{m_{k_1}} \sum_{j=1}^{m_{k_2}} \pi_{i,j}^{(k_1, k_2)} \cdot W^2(P(\phi_i^{(k_1)}, A), P(\phi_j^{(k_2)}, A)),$$

$$\bar{V}_W(A, \Pi^*) = \frac{1}{|\mathcal{I}_W|} \sum_{(k_1, k_2) \in \mathcal{I}_W} \sum_{i=1}^{m_{k_1}} \sum_{j=1}^{m_{k_2}} \pi_{i,j}^{(k_1, k_2)} \cdot W^2(P(\phi_i^{(k_1)}, A), P(\phi_j^{(k_2)}, A)).$$

For a Gaussian distribution $\phi \sim N(\mu, \boldsymbol{\Sigma})$, linear transform by matrix A yields a Gaussian distribution $P(\phi, A) \sim N(A^t \mu, A^t \boldsymbol{\Sigma} A)$. Let $\tilde{\boldsymbol{\Sigma}}_i^{(k)} = A^t \boldsymbol{\Sigma}_i^{(k)} A$. Note that the squared Wasserstein distance between $P(\phi_i^{(k_1)}, A)$ and $P(\phi_j^{(k_2)}, A)$ is

$$W^2(P(\phi_i^{(k_1)}, A), P(\phi_j^{(k_2)}, A)) = \left\| A^t \cdot \mu_i^{(k_1)} - A^t \cdot \mu_j^{(k_2)} \right\|^2 + \text{tr} \left[\tilde{\boldsymbol{\Sigma}}_i^{(k_1)} + \tilde{\boldsymbol{\Sigma}}_j^{(k_2)} - 2 \left(\left(\tilde{\boldsymbol{\Sigma}}_i^{(k_1)} \right)^{\frac{1}{2}} \tilde{\boldsymbol{\Sigma}}_j^{(k_2)} \left(\tilde{\boldsymbol{\Sigma}}_i^{(k_1)} \right)^{\frac{1}{2}} \right)^{\frac{1}{2}} \right]. \quad (12)$$

The second term in Eq. (12) for computing W^2 prevents us to convert Fisher’s ratio $r(a) = \widehat{V}_B(a, \Pi^*)/\widehat{V}_W(a, \Pi^*)$ into a form of Rayleigh-Ritz quotient, as that in Eq. (11). Consequently, the generalized eigenvalue problem cannot be applied in this case. We propose to approximate the true Wasserstein distance between Gaussian distributions by an upperbound denoted by \widehat{W} . Specifically, the upperbound of $W^2(\phi_1, \phi_2)$ is obtained by setting the corresponding optimal coupling $\boldsymbol{\pi}$ as $\widehat{\boldsymbol{\pi}}$ —the joint distribution of $Z_1 \sim \phi_1$ and $Z_2 \sim \phi_2$ under the independence assumption. Let

$$\widehat{W}^2(\phi_1, \phi_2) = E_{\widehat{\boldsymbol{\pi}}} \|Z_1 - Z_2\|^2 .$$

The following equations for computing \widehat{W}^2 are derived in Appendix B.

$$\begin{aligned} \widehat{W}^2(\phi_1, \phi_2) &= \|\mu_1 - \mu_2\|^2 + \text{tr}[\boldsymbol{\Sigma}_1 + \boldsymbol{\Sigma}_2] \\ &= \text{tr}[\boldsymbol{\Sigma}_1 + \boldsymbol{\Sigma}_2 + (\mu_1 - \mu_2) \cdot (\mu_1 - \mu_2)^t] \end{aligned} \quad (13)$$

$$\widehat{W}^2(P(\phi_1, A), P(\phi_2, A)) = \text{tr}[A^t \cdot (\boldsymbol{\Sigma}_1 + \boldsymbol{\Sigma}_2 + (\mu_1 - \mu_2) \cdot (\mu_1 - \mu_2)^t) \cdot A] . \quad (14)$$

Given the set of couplings Π^* , we approximate the Fisher’s ratio $r(A, \Pi^*)$ by

$$\widehat{r}(A, \Pi^*) = \frac{\widehat{V}_B(A, \Pi^*)}{\widehat{V}_W(A, \Pi^*)} ,$$

where

$$\begin{aligned} \widehat{V}_B(A, \Pi^*) &= \frac{1}{|\mathcal{I}_B|} \sum_{(k_1, k_2) \in \mathcal{I}_B} \sum_{i=1}^{m_{k_1}} \sum_{j=1}^{m_{k_2}} \pi_{i,j}^{(k_1, k_2)} \cdot \widehat{W}^2(P(\phi_i^{(k_1)}, A), P(\phi_j^{(k_2)}, A)), \\ \widehat{V}_W(A, \Pi^*) &= \frac{1}{|\mathcal{I}_W|} \sum_{(k_1, k_2) \in \mathcal{I}_W} \sum_{i=1}^{m_{k_1}} \sum_{j=1}^{m_{k_2}} \pi_{i,j}^{(k_1, k_2)} \cdot \widehat{W}^2(P(\phi_i^{(k_1)}, A), P(\phi_j^{(k_2)}, A)) . \end{aligned}$$

We emphasize that $\widehat{W}^2(\phi_1, \phi_2)$ is used as a substitute for $W^2(\phi_1, \phi_2)$ only after the optimal couplings in Π^* have been obtained using $W^2(\phi_1, \phi_2)$. Moreover, the usage of independent coupling $\widehat{\boldsymbol{\pi}}$ when computing \widehat{W}^2 applies solely at the level of individual Gaussian distributions. At the GMM level, the coupling between Gaussian components, $\boldsymbol{\pi}^{(k_1, k_2)} = (\pi_{i,j}^{(k_1, k_2)})_{i=1, \dots, m_{k_1}; j=1, \dots, m_{k_2}}$, is never assumed independent and must still be solved through OT. Thus, the use of \widehat{W}^2 does not alter the computation of $\boldsymbol{\pi}^{(k_1, k_2)}$. Its purpose is not to accelerate the calculation of the MAW distance between GMMs, but rather to make the Fisher’s ratio tractable.

Define

$$\begin{aligned}\hat{C}_B &= \frac{1}{|\mathcal{I}_B|} \sum_{(k_1, k_2) \in \mathcal{I}_B} \sum_{i=1}^{m_{k_1}} \sum_{j=1}^{m_{k_2}} \pi_{i,j}^{(k_1, k_2)} (\mu_i^{(k_1)} - \mu_j^{(k_2)}) \cdot (\mu_i^{(k_1)} - \mu_j^{(k_2)})^t \\ &+ \frac{1}{|\mathcal{I}_B|} \sum_{(k_1, k_2) \in \mathcal{I}_B} \left[\sum_{i=1}^{m_{k_1}} p_i^{(k_1)} \Sigma_i^{(k_1)} + \sum_{j=1}^{m_{k_2}} p_j^{(k_2)} \Sigma_j^{(k_2)} \right],\end{aligned}\quad (15)$$

$$\begin{aligned}\hat{C}_W &= \frac{1}{|\mathcal{I}_W|} \sum_{(k_1, k_2) \in \mathcal{I}_W} \sum_{i=1}^{m_{k_1}} \sum_{j=1}^{m_{k_2}} \pi_{i,j}^{(k_1, k_2)} (\mu_i^{(k_1)} - \mu_j^{(k_2)}) \cdot (\mu_i^{(k_1)} - \mu_j^{(k_2)})^t \\ &+ \frac{1}{|\mathcal{I}_B|} \sum_{(k_1, k_2) \in \mathcal{I}_W} \left[\sum_{i=1}^{m_{k_1}} p_i^{(k_1)} \Sigma_i^{(k_1)} + \sum_{j=1}^{m_{k_2}} p_j^{(k_2)} \Sigma_j^{(k_2)} \right].\end{aligned}\quad (16)$$

As in the discrete case, the between-class variation $\hat{V}_B(A, \Pi^*)$ and the within-class variation $\hat{V}_W(A, \Pi^*)$ are computed using the following equations (derivations are provided in Appendix C):

$$\hat{V}_B(A, \Pi^*) = \text{tr}(A^t \hat{C}_B A) \quad (17)$$

$$\hat{V}_W(A, \Pi^*) = \text{tr}(A^t \hat{C}_W A). \quad (18)$$

Based on Eq.(17) and (18),

$$\hat{r}(a, \Pi^*) = \frac{a^t \hat{C}_B a}{a^t \hat{C}_W a}, \quad (19)$$

which is the Rayleigh-Ritz quotient.

The ratio in Eq. (11) or Eq. (19) is essentially the Rayleigh-Ritz quotient with matrices C_B (or \hat{C}_B) and C_W (or \hat{C}_W). Without loss of generality, we discuss in terms of \hat{C}_B and \hat{C}_W . Note that both matrices are semi-positive definite, and in practice, usually positive definite. Here, \hat{C}_B and \hat{C}_W play a similar role as the between-class covariance and within-class covariance matrix in LDA. The solution to Fisher's optimization applies likewise. Specifically, let $\hat{C}_W = \left(\hat{C}_W^{\frac{1}{2}}\right)^t \cdot \hat{C}_W^{\frac{1}{2}}$ and $\hat{C}_B^* = \left(\hat{C}_W^{-\frac{1}{2}}\right)^t \hat{C}_B \hat{C}_W^{-\frac{1}{2}}$. Use change of variables and define $b = \hat{C}_W^{\frac{1}{2}} \cdot a$. Then Fisher's ratio becomes

$$r(b, \Pi^*) = \frac{b^t \hat{C}_B^* b}{b^t b},$$

which is maximized using eigen-decomposition of \hat{C}_B^* . Assume that the eigenvalues are in descending order and the corresponding eigenvectors are $(v_1^*, v_2^*, \dots, v_d^*)$. Then $b = v_1^*$ maximizes $r(b, \Pi^*)$. Consequently, $a = \hat{C}_W^{-\frac{1}{2}} \cdot v_1^*$ maximizes $r(a, \Pi^*)$.

In light of the above discussion, we iterate between computing couplings $\boldsymbol{\pi}^{(k_1, k_2)}$, $(k_1, k_2) \in \mathcal{I}_B \cup \mathcal{I}_W$ given a and optimizing a under the given couplings. The solution of squared MAW

distances $\widetilde{W}^2(P(\mathcal{G}_{k_1}, a), P(\mathcal{G}_{k_2}, a))$ includes $\pi^{(k_1, k_2)}$'s. For discrete distributions, the squared Wasserstein distances $W^2(P(\mathcal{Q}_{k_1}, a), P(\mathcal{Q}_{k_2}, a))$ are computed instead.

To start the iteration, we initialize $\pi^{(k_1, k_2)}$'s based on the original data (no dimension reduction). The two index sets \mathcal{I}_B and \mathcal{I}_W are pre-selected. We will provide a brief explanation of the method used to determine \mathcal{I}_B and \mathcal{I}_W shortly.

Similarly as with the conventional Fisher's optimization, if the reduced dimension is more than one, we let $b_i = v_i^*$, $i = 1, \dots, d'$, where $d' < d$ is the desired dimension. The b_i 's are orthonormal. Following the terminology in LDA, we define

$$a_i = C_W^{-\frac{1}{2}} \cdot b_i . \quad (20)$$

as the *discriminant coordinates* or *canonical variates* axes.

In contrast to Fisher's classical solution for LDA, the discriminant coordinates a_i in our approach are not computed by a closed form but are instead updated iteratively in tandem with the coupling weights. Consider the scenario where $d' > 1$. In this case, we define the matrix A as $A = (a_1, \dots, a_{d'})$. Next, we compute the projection $P(\mathcal{Q}_k, A)$ for each $k = 1, \dots, n$. These projections are then used to calculate pairwise Wasserstein distances and to update the couplings in Π^* , based on which A will be updated again. When an orthonormal projection is required, the OTAF method is adjusted accordingly. Specifically, after determining a_i , $i = 1, \dots, d'$, an orthonormal span for the subspace spanned by a_i 's is identified and the orthonormal basis are taken as a_i 's instead.

We now describe the method for determining the index sets \mathcal{I}_B and \mathcal{I}_W , which correspond to between-class and within-class pairs, respectively. For each instance \mathcal{G}_k , $k = 1, \dots, n$, we calculate its average squared MAW distance (in the original dimension) to every other instance within the same class, denoted as δ_k . Additionally, we compute its average squared MAW distance to instances from different classes, denoted as δ'_k . Define *discriminant distance ratio* $\gamma_k = \delta'_k / \delta_k$. A higher γ_k value indicates that \mathcal{G}_k is, on average, more distant from instances in different classes compared to those in the same class, suggesting that \mathcal{G}_k is easier to classify. Rather than considering all pairs $(\mathcal{G}_{k_1}, \mathcal{G}_{k_2})$, we focus on the more challenging cases as indicated by γ_k . We rank γ_k 's and select a specific proportion—say, α percent—of the values with the smallest γ_k . In our experiment, we set α to $1/3$. We denote the set of selected k values as \mathcal{K}_α . For simplicity, define $\mathcal{K} = \{1, \dots, n\}$. Then $\mathcal{I}_B = \{(k_1, k_2) : k_1 \in \mathcal{K}_\alpha, k_2 \in \mathcal{K}, Y_{k_1} \neq Y_{k_2}\}$, and $\mathcal{I}_W = \{(k_1, k_2) : k_1 \in \mathcal{K}_\alpha, k_2 \in \mathcal{K}, Y_{k_1} = Y_{k_2}\}$.

3.4 A unified algorithm

Next, we articulate the OTAF algorithm in a manner applicable to both discrete distributions, as per the Wasserstein distance, and GMMs, as per the MAW distance. To streamline the discussion, we equate a discrete distribution $\{(p_i, x_i), i = 1, \dots, m\}$ to a GMM with m components, $\{(p_i, \phi_i), i = 1, \dots, m\}$, where p_i represents the prior probability of the i -th component, and ϕ_i is a Gaussian distribution with mean $\mu_i = x_i$ and a zero covariance matrix $\Sigma_i = \mathbf{0}$. In this representation, the MAW distance between GMMs aligns with the Wasserstein distance between discrete distributions. Importantly, when the covariance matrices are entirely degenerated, we have $W^2(\phi_i, \phi_j) = \widetilde{W}^2(\phi_i, \phi_j) = \|\mu_i - \mu_j\|^2$, that is, the

Wasserstein distance $W(\phi_i, \phi_j)$ and the upperbound distance $\widehat{W}(\phi_i, \phi_j)$ for the Gaussian distributions are identical to the Euclidean distance between the mean vectors $\|\mu_i - \mu_j\|$. Moreover, with $\Sigma_i = \mathbf{0}$, \hat{C}_B and \hat{C}_W in Eqs. (15) and (16) simplify to C_B and C_W in Eqs. (7) and (8), respectively, since the second terms in Eqs. (15) and (16) vanish. In summary, treating the support points of a discrete distribution as degenerated Gaussian components does not alter the algorithm. We thus describe the OTAF algorithm, presented in Algorithm 1, for GMMs. It is worth noting that Algorithm 1 does in fact make use of the class labels Y_k . Specifically, the labels are required to determine \mathcal{I}_B and \mathcal{I}_W , which specify the between-class and within-class pairs of indices. Beyond this role, the dependence on class labels is not explicitly reflected in the remaining steps of the algorithm.

Algorithm 1: OTAF

- Input:** A collection of GMMs $\mathcal{G}_k = \{(p_i^{(k)}, \phi_i^{(k)}), i = 1, \dots, m_k\}$, $\phi_i^{(k)} \sim N(\mu_i^{(k)}, \Sigma_i^{(k)})$, and their class labels Y_k , $k = 1, \dots, n$;
Hyperparameters: d' (the reduced dimension), κ , $\bar{\kappa}$ (the minimum and maximum numbers of iterations), ϵ (threshold for termination, e.g., $1.0e - 4$).
- 1: Determine \mathcal{I}_B and \mathcal{I}_W based on the discriminant distance ratios (Section 3.2).
 - 2: $\mathbf{I}_{d \times d} \rightarrow A$, where $\mathbf{I}_{d \times d} \in \mathbb{R}^{d \times d}$ is the identity matrix.
 - 3: $1 \rightarrow \tau$, $\infty \rightarrow \eta$, compute the Fisher's ratio $r(A)$, $r(A) \rightarrow \rho^\tau$.
 - 4: **while** $\tau < \kappa$ or $(\eta > \epsilon$ and $\tau < \bar{\kappa})$ **do**
 - 5: Compute the projected GMMs: $P(\mathcal{G}_k, A)$, $k = 1, \dots, n$. Solve OT couplings $\pi^{(k_1, k_2)}$ for $P(\mathcal{G}_{k_1}, A)$ and $P(\mathcal{G}_{k_2}, A)$, $(k_1, k_2) \in \mathcal{I}_B \cup \mathcal{I}_W$.
 - 6: Compute \hat{C}_B by Eq. (15) and \hat{C}_W by Eq. (16). Let $(\hat{C}_W^{-\frac{1}{2}})^t \hat{C}_B \hat{C}_W^{-\frac{1}{2}} \rightarrow C_B^*$.
 - 7: Solve the eigenvectors $(v_1^*, v_2^*, \dots, v_d^*)$ of C_B^* (descending eigenvalues). Let $\hat{C}_W^{-\frac{1}{2}} \cdot v_i^* \rightarrow a_i$, $i = 1, \dots, d'$.
 - 8: If orthonormal basis is required, set A to be the orthonormal basis spanning $(a_1, \dots, a_{d'})$, otherwise $(a_1, \dots, a_{d'}) \rightarrow A$.
 - 9: $\tau + 1 \rightarrow \tau$
 - 10: Compute $r(A)$, $r(A) \rightarrow \rho^\tau$, and $(\rho^\tau - \rho^{\tau-1})/\rho^{\tau-1} \rightarrow \eta$.
 - 11: **end while**
- return** Projection matrix A , $A \in \mathbb{R}^{d \times d'}$.
-

To establish a criterion for terminating the iterative process, we evaluate Fisher's ratio $r(A)$ in each round and compare the previous A with the current updated one. The iteration is stopped when the relative increase in this ratio falls below a predetermined threshold, for instance, 10^{-4} . Empirical evidence from our experiments indicates that convergence under this criterion typically occurs at a rapid pace.

To better understand the theoretical underpinnings of the OTAF algorithm, we focus on the simpler scenario of discrete distributions and the optimization process for a single direction $a \in \mathbb{R}^d$. By its definition, $r(a) = r(a, \Pi^*)$, where Π^* is the set of optimal couplings under the projection a . A theoretical challenge comes from the fact we cannot definitively assert that Π^* is the maximizer of $r(a, \Pi)$ for all feasible coupling sets Π . It is evident that

$\bar{V}_B(a) = \bar{V}_B(a, \Pi^*) \leq \bar{V}_B(a, \Pi)$, and similarly, $\bar{V}_W(a) = \bar{V}_W(a, \Pi^*) \leq \bar{V}_W(a, \Pi)$. Yet, the inequality $r(a, \Pi^*) \geq r(a, \Pi)$, where $r(a, \Pi) = \bar{V}_B(a, \Pi)/\bar{V}_W(a, \Pi)$, may not hold.

In Appendix D, we establish a relatively modest result pertaining to this issue, which is stated in Theorem 1. In practical applications, especially when the reduced dimension $d' > 1$, we typically observe that the algorithm converges swiftly after a few iterations, followed by minor oscillations over an extended period. In contrast, for $d' = 1$, the algorithm shows a consistent ascending trend and reaches convergence rapidly. This phenomenon and its implications are thoroughly examined in Section 4.5.

Theorem 1 *For discrete distributions, if we assume $r(a) \geq r(a, \Pi)$, where Π contains valid couplings, the OTAF algorithm for maximizing $r(a) = \frac{\bar{V}_B(a)}{\bar{V}_W(a)}$, $a \in \mathbb{R}^d$ generates a sequence of objective values $\{r(a_\tau)\}_{\tau \geq 1}$ that is non-decreasing and bounded above, guaranteeing convergence to a set of stationary points. Furthermore, if (a_τ, Π_τ) is not a stationary point of the objective $r(a)$, then the iteration guarantees a strictly ascending step, $r(a_{\tau+1}) - r(a_\tau) > 0$.*

In the case of GMMs, as the Wasserstein distance between Gaussian components is replaced by its upper bound, it is even harder to provide a theoretical guarantee for the algorithm. We will again investigate the convergence characteristic of the algorithm in this scenario via experiments.

The computational cost of OTAF is dominated by solving the OT problems. Each OT problem involves a number of variables that grows quadratically with the number of support points in the distribution (in the case of GMMs, the number of mixture components). Consequently, the overall runtime is strongly influenced by the support sizes of the distributions. The number of OT problems to be solved per iteration depends on $|\mathcal{I}_B \cup \mathcal{I}_W|$, which in practice is data-dependent; in our implementation, approximately one third of the “easiest-to-misclassify” instances are used to form \mathcal{I}_B and \mathcal{I}_W . Although our current implementation is single-threaded, OTAF is highly amenable to parallelization because the OT couplings between different instance pairs are independent and can be computed concurrently.

To provide a more quantitative perspective on scaling behavior, the theoretical computational complexity of OTAF can be expressed as $O(|\mathcal{I}_B \cup \mathcal{I}_W| f(m^2))$, where m denotes the support size and $f(\cdot)$ characterizes the cost of the OT solver as a function of the number of variables. The interior-point optimization method implemented in the MOSEK package, which we employ to solve OT, typically exhibits a slightly superlinear dependence on the number of variables. However, our simulation study (Section 4.3) empirically shows that the total computation time grows approximately linearly with the number of variables, thus roughly quadratically with the support size.

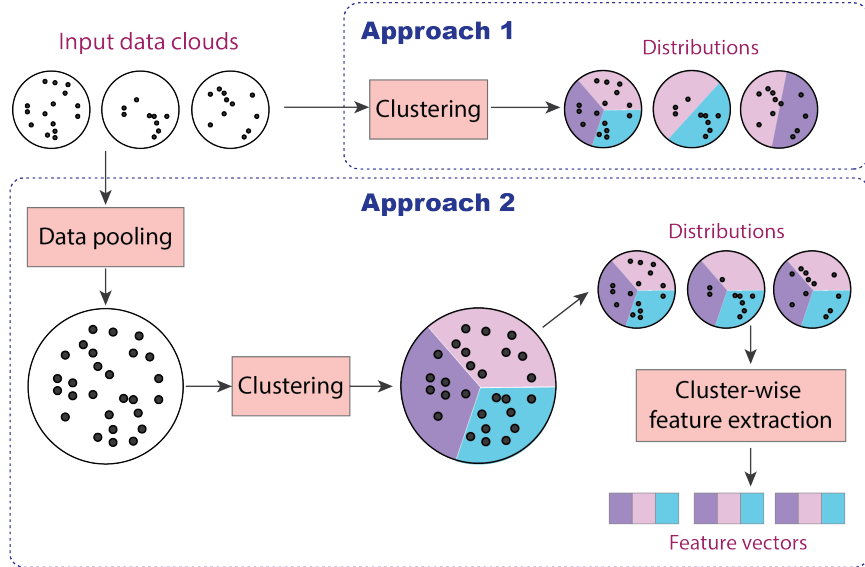


Figure 1: Two approaches for representing data clouds. Approach 1: data points in each instance (a data cloud) are clustered separately. Approach 2: data points in all instances are pooled and clustered together with coherent cluster labels assigned. Cluster-wise feature extraction can be performed to create vector representations.

4 Experiments

4.1 Data Preparation

Our experiments involve three real datasets, each comprising instances that contain a set of data points. For example, an instance can be a patient characterized by a set of feature vectors, each containing measurements of individual cells in the patient’s tissue sample. Typically, a tissue sample from one patient contains numerous cells. In the discussion below, the terms “data cloud” and “subject” are used interchangeably to refer to an instance: the former highlights the structural form of the data, whereas the latter is more common in biomedical contexts.

Each data cloud is processed to generate a GMM representation for the corresponding subject. The resulting GMMs vary depending on the estimation method and the assumed number of components. We examine multiple modeling schemes with different component counts; consequently, each original dataset gives rise to several collections of GMMs, each treated as an independent dataset in our experiments. Every collection corresponds to a specific modeling scheme and a fixed number of components. In summary, we begin with three original datasets, from which eight variants are derived per dataset, yielding a total of 24 datasets (each containing a collection of GMMs), all used to evaluate our method.

In particular, for every subject in the study, we generated eight different GMMs using two primary clustering approaches: the “separate” method and the “combined” method. These two approaches, the former being “Approach 1” and the latter “Approach 2”, are illustrated in Figure 1. In the combined approach, cells from all subjects are pooled into a single dataset, which is then subjected to clustering. This results in consistent cluster labels

across all subjects. For each subject, we estimate the Gaussian mean and covariance for each cluster based on the assigned cluster labels to their data points, subsequently forming the GMM. The proportion of points in a cluster is taken as the prior probability of the corresponding Gaussian component. It is important to note that some subjects might not have data points in certain clusters; these clusters only contain points from other subjects. Consequently, the number of Gaussian components for such a subject will be fewer than the total number of clusters identified in the combined dataset. On the other hand, in the separate method, we perform clustering on the points within each subject individually. After clustering, the GMM is formed likewise.

In both the combined and separate clustering schemes, we set the number of components in the GMMs as 3, 5, 7, and 10. For the brevity of discussion, denote the number of components in a GMM by ζ . We also adopt the following naming convention. Take GMM-C-3 as an example. It refers to a GMM with $\zeta = 3$ which is obtained by the combined clustering scheme. In contrast, GMM-S-3 indicates that the separate clustering scheme is used. If a subject’s point count is relatively low, we adjust the number of components to a smaller value than the initially set number. While our method is also applicable to discrete distributions (considered as a special case of GMMs in our algorithm description), directly working with the entire data cloud of each subject is often impractical due to the vast number of points in each cloud. Clustering serves not only to reduce computational demands in subsequent processes but also to enhance the robustness of the analysis against noise in the data. The clusters thus formed can often provide a more effective representation of the original data cloud. However, the application of clustering brings its own set of challenges. A common difficulty lies in determining the optimal number of components for a GMM. Therefore, it is beneficial to have methodologies that remain robust despite variations in the GMM representation. To address this, we generated GMMs with varying numbers of components and evaluated the prediction accuracy of each model across different algorithms in our experiments.

By using both combined and separate clustering schemes in our study, we can compare our method with traditional vector-based approaches. In conventional machine learning applications for vector data, a common strategy for handling data clouds involves transforming them into vectors based on the combined clustering scheme. We describe the details of the conversion process in Section 4.2. In practical scenarios, factors such as privacy concerns may render the pooling of data for clustering infeasible. Additionally, there are inherent limitations to data pooling. For instance, when applying a learned prediction function to a new test subject, the data points of this subject must be clustered according to the same partitioning rules derived from the training data. This necessitates storing the partitioning rules as part of the learned model, which can be cumbersome. Moreover, from a learning perspective, clustering each subject’s data separately is often more effective in capturing distributions that are specifically tailored to each individual subject. For example, if a patient has a unique, small subset of cells, separate clustering is more likely to identify and characterize this distinct group. In contrast, when cells from all patients are clustered together, such a small group may be overshadowed or its members might be misclassified as outliers in other larger clusters. This highlights the importance of considering individual patient variability in the clustering process to ensure that unique characteristics

are not overlooked. As will be discussed below, these aforementioned limitations of data pooling and aligned clustering have been reflected by experimental results.

4.2 Evaluation Method

To perform classification based on pairwise distances alone, we employ the kernel version of the pseudo-mixture model developed by Qiao and Li (2016). For each class l , $l = 1, \dots, M$, a pseudo-density denoted by \mathcal{M}_l is formed based on distances. Essentially, a pseudo-density is a conceptually formulated density function on a metric space, on the notion of distance-preserving mapping from a metric space to a Euclidean space, as detailed in the work of (Qiao and Li, 2016). Suppose the GMMs in a class are \mathcal{G}_j , $j \in \mathcal{I}_l$, where \mathcal{I}_l is a set of indices containing the instances that belong to class l . The pseudo-density computed at a GMM \mathcal{G} is

$$\psi(\mathcal{G} | \mathcal{M}_l) = \sum_{j \in \mathcal{I}_l} \frac{1}{|\mathcal{I}_l|} \left(\frac{1}{\sqrt{\pi b}} \right)^{2s} e^{-\frac{\bar{w}^2(\mathcal{G}, \mathcal{G}_j)}{b}}, \quad (21)$$

where s is a shape parameter and b is a scale parameter, both are shared across the classes. Details on the estimation of s and b are referred to (Qiao and Li, 2016). Suppose the prior probabilities of class l is α_l , $\sum_{l=1}^M \alpha_l = 1$. Then the posterior probability for class l is $P(Y = l | \mathcal{G}) \propto \alpha_l \psi(\mathcal{G} | \mathcal{M}_l)$. If dimension reduction is applied, we need to replace \mathcal{G} and \mathcal{G}_j 's by the marginal distributions in the reduced dimensions.

In our study on the real datasets, given the limited number of subjects, we evaluated performance using leave-one-out classification accuracy and Area Under Curve (AUC), both in the range of $[0, 1]$ with a higher value indicating better performance. We compared these results with several established classification algorithms: Support Vector Machine (SVM), Random Forest (RF), Logistic Regression (LR), and Multi-layer Perceptron (MLP) neural networks. Our proposed method is referred to as *Canonical Variates in Wasserstein space* (CVW), with two variants: CVW-C, applying CVW to Gaussian Mixture Models (GMMs) created using the combined clustering approach, and CVW-S, employing CVW with GMMs derived from the separate clustering scheme. The CVW method first apply the OTAF algorithm to reduce the dimension to a specified value. Then we form the pseudo-mixture model in Eq. (21) based on the Wasserstein distance between GMMs in the dimension reduced space. For one dataset described in Section 4.4.1, we also evaluated the performance of the pseudo-mixture model in the original space. We refer to this method simply as *Pseudo-Mixture Model* (PMM).

To compare with vector-based classification methods, including SVM, RF, LR, and MLP, we convert the distributional data of each subject into a feature vector, and then the models are trained at the subject level. Similarly to the CVW approach, we do not assign subject-level class labels to individual points within each subject, nor do we perform classification at the point level. In biomedical applications, subjects belonging to different classes often contain overlapping cell types, sometimes partially, sometimes entirely, with class differences arising primarily from variations in the compositional mixture. Moreover, the cell types themselves, unlike subject-level classes, may not be known.

The conversion process starts with clustering applied to the combined data across subjects so that the clusters for each subject are aligned by setup. As described earlier, we obtain a component-aligned GMM representation for each subject, denoted by $\mathcal{G}_k = \{(p_i^{(k)}, \phi_i^{(k)}), i = 1, \dots, m\}$, where $\phi_i^{(k)} \sim N(\mu_i^{(k)}, \Sigma_i^{(k)})$, $k = 1, \dots, n$. For each Gaussian component i , we use $p_i^{(k)}$ (referred to as the cluster proportion), $\mu_i^{(k)}$ (referred to as the cluster mean), and the diagonal elements of $\Sigma_i^{(k)}$ (i.e., the variances of each dimension) as features, and concatenate these features across all Gaussian components. The total dimensionality of the resulting feature vector is $m(1 + 2d)$. As with CVW-C, results are reported for different numbers of Gaussian components. When a subject has a missing cluster, the corresponding proportion is set to zero, and the cluster mean is replaced by the mean over the entire dataset. We also examined alternative feature combinations, such as using only cluster proportions, only cluster means, or both proportions and means. The Supplementary Material presents accuracy and AUC results for these variants. No particular combination of features yields universally superior performance; however, using all $m(1 + 2d)$ features achieves the most competitive results on average. For consistency, all results presented below are based on this full feature set. For the SVM, RF, and LR models, we experimented with various hyperparameter settings and report only the best performing configurations. For MLP, we used a fully connected two-layer architecture, with layer widths determined according to common practice based on data dimensionality and sample size. Specifically, for small data size (≤ 100), the first layer contains 8 neurons and the second contains 4.

4.3 Simulated Data

We first demonstrate the application of OTAF on simulated data and compare its classification performance and computational efficiency using two types of distributional representations: GMMs and discrete distributions.

In this simulation study, we perform binary classification on distributional subjects. The prior probabilities for the two classes are set to 0.6 and 0.4. Each subject (i.e., a data cloud) consists of a random sample of 1,200 eight-dimensional vectors, referred to as data points. The generative model for each subject varies, but subjects within the same class are drawn from slightly perturbed versions of a common base model. The base models for both classes are GMMs with four components. Among the eight dimensions, two exhibit class-dependent differences, while the remaining six are independent of the class label. We refer to the class-dependent dimensions as signal dimensions and the others as noise dimensions.

After generating data for each subject, we apply a random, subject-specific rotation matrix to the eight-dimensional data. Consequently, the two signal dimensions form a randomly oriented two-dimensional signal subspace for each subject. Although the identity of this signal subspace is known, OTAF operates without access to it. For each class, 500 subjects are generated. From the pool of 1,000 subjects, we then created 20 datasets, each containing 50 subjects with class proportions (0.6, 0.4). Within each dataset, subjects are sampled without replacement. Details of the base GMMs and the per-subject perturbations are provided in the Supplementary Materials.

Figure 2 illustrates the simulated data before random rotation is applied to each sub-

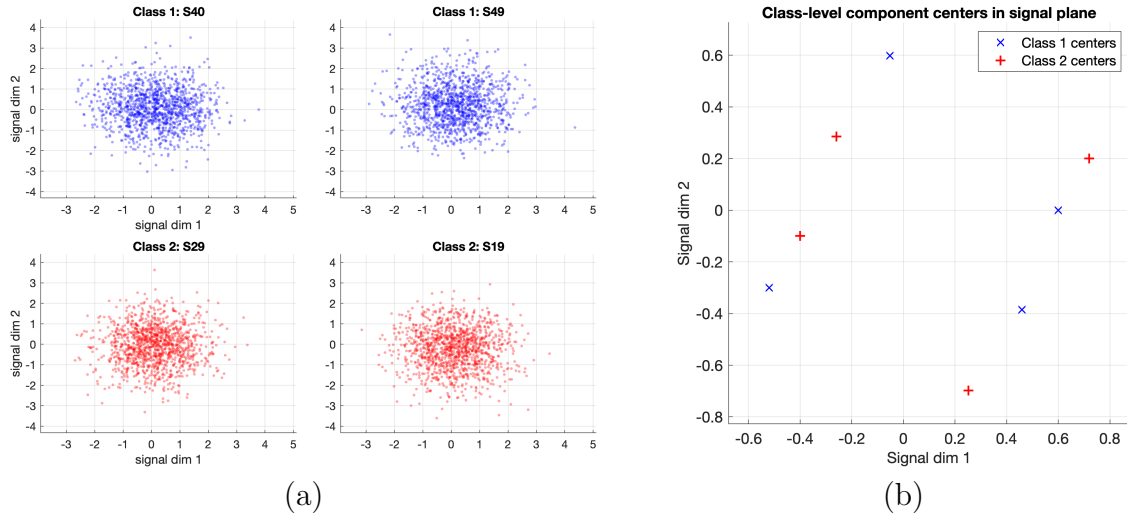


Figure 2: Illustration of the simulated data. (a) Scatter plots of the two signal dimensions for example subjects. The top row shows two subjects from Class 1, and the bottom row shows two subjects from Class 2. The distributions of the two classes exhibit substantial overlap. (b) The two signal dimensions are shown for the GMM component means of the two base models used in each class. The locations of these component means highlight the underlying differences between the classes.

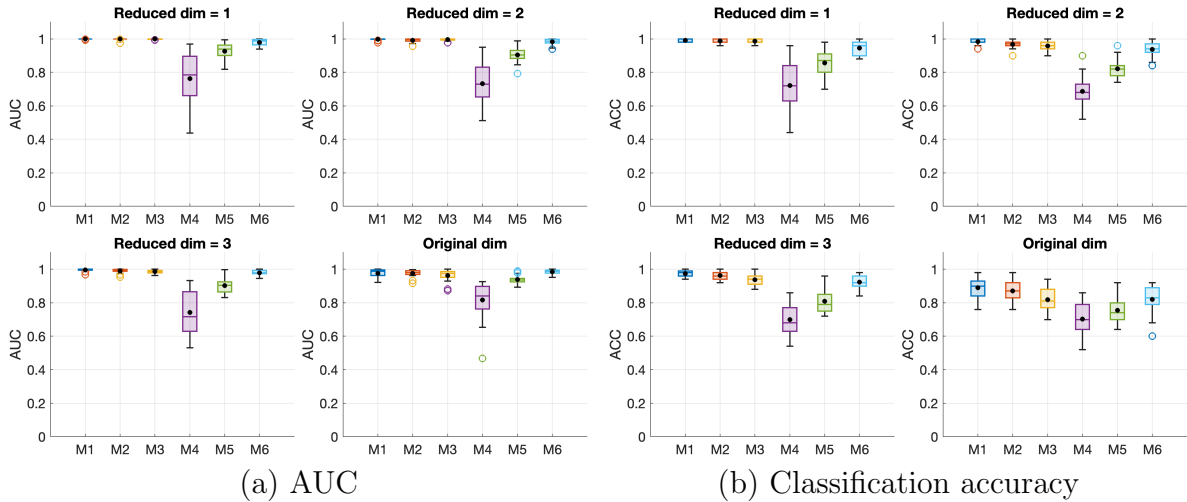


Figure 3: Classification performance on the simulated datasets. (a) AUC and (b) Classification accuracy. Each boxplot summarizes results from 20 simulated datasets, with black dots indicating the average values. Each panel corresponds to either the original or a reduced feature dimension, and contains six boxplots representing the six data representation models: GMMs with $\zeta = 3, 4,$ and 6 components (M1–M3), and discrete distributions with 50, 100, and 200 support points (M4–M6).

ject. In Figure 2(a), scatter plots of the two signal dimensions are shown for example subjects: the top row corresponds to two subjects from Class 1, and the bottom row to two subjects from Class 2. Each subject’s data points are plotted in a separate panel, revealing within-class variability and substantial overlap between the two classes. At first glance, the distributions of the two classes appear largely similar. Figure 2(b) shows the GMM component means for the two base models associated with each class, which highlight the underlying distributional differences between them.

To construct the distributional representation for each subject, we considered six variants: GMMs fitted with the number of components $\zeta = 3, 4,$ and $6,$ respectively, and discrete representations obtained by randomly sampling (without replacement) subsets of $50, 100,$ and 200 data points. The latter three cases serve as discrete approximations of the underlying distributions. We assess the classification performance of OTAF followed by PMM for each dataset using 10-fold cross-validation AUC and classification accuracy. Figure 3 shows boxplots of AUC and accuracy for different distribution-representation models: GMMs with $\zeta = 3, 4,$ and 6 components, and discrete distributions with $50, 100,$ and 200 support points. Each boxplot summarizes results from 20 simulated datasets, with each black dot inside the box representing the mean value obtained from 10-fold cross-validation for one simulated dataset. Each panel in Figures 3(a) and (b) corresponds to a reduced dimension ($1, 2,$ or 3) or the original feature dimension.

When no dimension reduction is applied, the discrete distribution with 200 support points achieves AUC values comparable to those of the GMMs, but moderately lower classification accuracy than the GMMs with $\zeta = 3$ or 4 . As shown later, the computational cost of using discrete distributions is substantially higher. The performance of discrete distributions varies noticeably with support size, with the 200 -point model performing much better than the 50 -point model. In contrast, GMM performance is relatively stable across different numbers of components, underscoring the robustness of GMMs as distributional representations. This sensitivity of performance to support size becomes even more evident when dimension reduction is applied. In terms of AUC, discrete-distribution performance generally degrades after dimension reduction, with the decline being more pronounced at smaller support sizes. In terms of accuracy, a moderate improvement is observed for support sizes of 100 and $200,$ while performance at 50 points remains largely unchanged. In contrast, for GMM-based representations, both AUC and accuracy improve after dimension reduction, and GMM-based models consistently outperform their discrete-distribution counterparts, even those with 200 support points.

In Table 1, we report the computation times for dimension reduction and classification under different settings. All experiments were performed on an Apple Mac Mini equipped with an M2 Pro processor (3.5 GHz, 16 GB unified memory), running macOS Sonoma 14.7 and MATLAB R2024a. When the original feature dimension was used, the reported time reflects only the PMM classification stage. In any case, the time reported is the total over 10-fold cross-validation. When dimension reduction was applied, for the GMM-based representations, approximately 13% of the total runtime was attributable to PMM and the remainder to OTAF; for the discrete-distribution representations, about 6% of the time was due to PMM and the rest to OTAF.

The dominant factor affecting runtime is the number of components (for GMMs) or sup-

| Dim | GMM | | | Discrete distribution | | |
|-------|------------|------------|------------|-----------------------|---------------|-----------------|
| | 3 | 4 | 6 | 50 | 100 | 200 |
| Orig. | 4.4 (0.0) | 5.6 (0.0) | 9.0 (0.1) | 61.2 (3.3) | 231.5 (9.8) | 1020.5 (33.5) |
| 1 | 34.0 (0.5) | 40.0 (1.2) | 54.0 (0.9) | 824.0 (15.9) | 3140.0 (35.9) | 13518.0 (118.2) |
| 2 | 35.0 (0.4) | 42.0 (0.8) | 59.0 (1.1) | 1063.0 (20.8) | 4058.0 (52.9) | 17101.0 (114.9) |
| 3 | 37.0 (0.4) | 45.0 (0.7) | 66.0 (1.1) | 1076.0 (15.8) | 4100.0 (42.7) | 17292.0 (94.4) |

Table 1: Average runtime (in seconds) with standard deviation (shown in parenthesis), computed over 20 sample datasets. Each dataset was evaluated under six representation schemes: GMMs with $\zeta = 3, 4,$ and 6 components, and discrete distributions with $50, 100,$ and 200 support points. The reported runtime corresponds to the total computation time for 10-fold cross-validation, including both the application of dimension reduction and classification using PMM.

port points (for discrete distributions), collectively referred to as the support size hereafter. The computational cost of the OT optimization used to compute Wasserstein distances, specifically, the interior-point method implemented in the MOSEK package, grows roughly quadratically with the distribution’s support size. This scaling arises because the number of variables in the OT problem also increases quadratically with support size. Figure 4 plots runtime against support size for reduced dimensions 1, 2, and 3. A quadratic fit in each case yields adjusted R^2 values exceeding 0.999. Fits using higher-degree polynomials (degrees 3 and 4) produce negligible coefficients for the cubic and quartic terms, confirming that computation time increases approximately quadratically with support size.

4.4 Real Datasets

4.4.1 Pulmonary fibrosis data analysis

We experiment with a single-nucleus sequencing data of (Habermann et al., 2020) related to pulmonary fibrosis (PF). This dataset comprises 20 cases and 10 controls. A recent publication has highlighted that the majority of significant signals are observed in epithelial cell types, specifically SCG3A2+, AT2, Basal, MUC5B+, and AT1 Zhang and Guo (2022). In our analysis, we focus on SCG3A2+ cell types. We downloaded the data from https://github.com/mqzhanglab/BSDE_pipeline/tree/main/data/IPF. The number of SCG3A2+ cells per individual subject ranges from 1 to 663. Since the number of cells is relatively small, we select the top 30 highly variable genes for our analysis. If the number of cells per sample is below 10, we model the cells by a single 30-dimensional Gaussian distribution, so the sample mean and covariance of the cells are the estimates of the Gaussian mean and covariance matrix. For the case where there is only one cell in the sample, we use that cell as the estimate of the Gaussian mean, and estimate the covariance by the sample covariance matrix of ten perturbed sample points generated by adding to that point Gaussian noise (zero mean and standard deviation 0.1), similarly as the practice in Lin et al. (2023). Otherwise, we construct a GMM for the sample based on k-means clustering, as explained in the previous subsection.

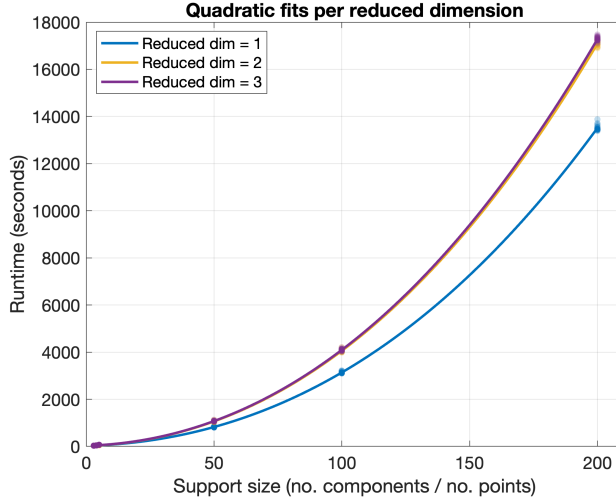


Figure 4: Computation time versus the distribution support size when the reduced dimension is 1, 2, and 3 respectively. Each curve shows the fitted polynomial relationship between runtime and support size. A quadratic model provides an excellent fit in all cases, with adjusted R^2 values above 0.999.

In Figure 5(a), we compare the performance in terms of classification accuracy and AUC achieved by CVW and PMM across different numbers of Gaussian components and the two schemes of clustering (CVW-C versus CVW-S). For PMM, performance based on GMM-S’s (separate clustering) is better than that from GMM-C’s (combined clustering). This observation may be attributed to better fitting of GMM by separate clustering. When dimension reduction is applied, however, the difference in AUC or accuracy becomes negligible. We also note that for both PMM and CVW, the performance is stable across different number of components in the GMM. In addition, dimension reduction to a single dimension yields consistently better results than classification in the original dimension. The improvement is remarkable in terms of accuracy. By AUC, the improvement from dimension reduction is most noticeable for GMMs formed based on combined clustering.

In Figure 5(b), we compare CVW-S and CVW-C with SVM, RF, LR, and MLP. Note that the GMMs used by these four methods are of the GMM-C type, the same as those used by CVW-C. For SVM, linear kernel is the best among RBF and polynomial at degree 3. For LR, we use elastic net to estimate the logistic model. SVM is most sensitive to the number of components in GMMs and performs substantially worse than other methods when that number is 3 or 5. In terms of both accuracy and AUC, CVW-S and CVW-C achieve similar results and outperform the four benchmark methods. As shown in the legends on the right hand side of the plots, when averaged over $\zeta \in \{3, 5, 7, 10\}$, CVW-S achieves the highest AUC. In terms of average accuracy, CVW-S and CVW-C reach the same level, and are considerably better than RF and MLP (the second best). As shown by the standard deviation of the AUC or accuracy in the parenthesis, CVW-S and CVW-C perform most stably when ζ changes.

To further study the sensitivity of CVW to the number of components in GMM, we conduct the following study where the GMMs of training and test subjects have different

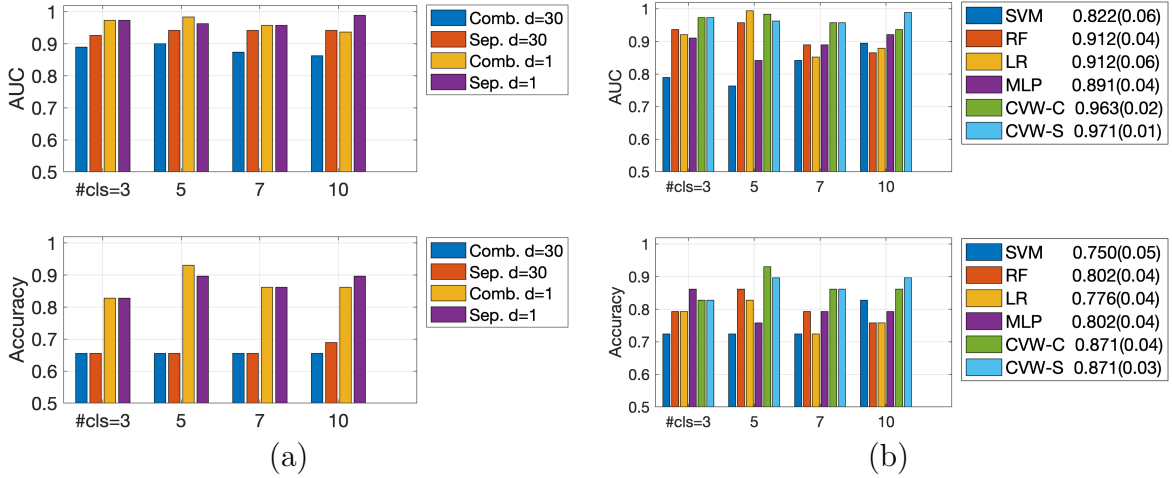


Figure 5: Performance comparison on the PF dataset measured by AUC and classification accuracy. (a) Results obtained from GMMs generated by the combined clustering and separate clustering schemes. The number of components in GMMs varies over $\{3, 5, 7, 10\}$. The original dimension is 30. With dimension reduction, one canonical variate is used. (b) Results obtained by vector-based algorithms SVM, RF, LR, and MLP are compared with CVW-C and CVW-S. In the legends on the right hand side of the plot, the average performance over the four different numbers of components is shown for each algorithm, and the value inside the parenthesis is the standard deviation.

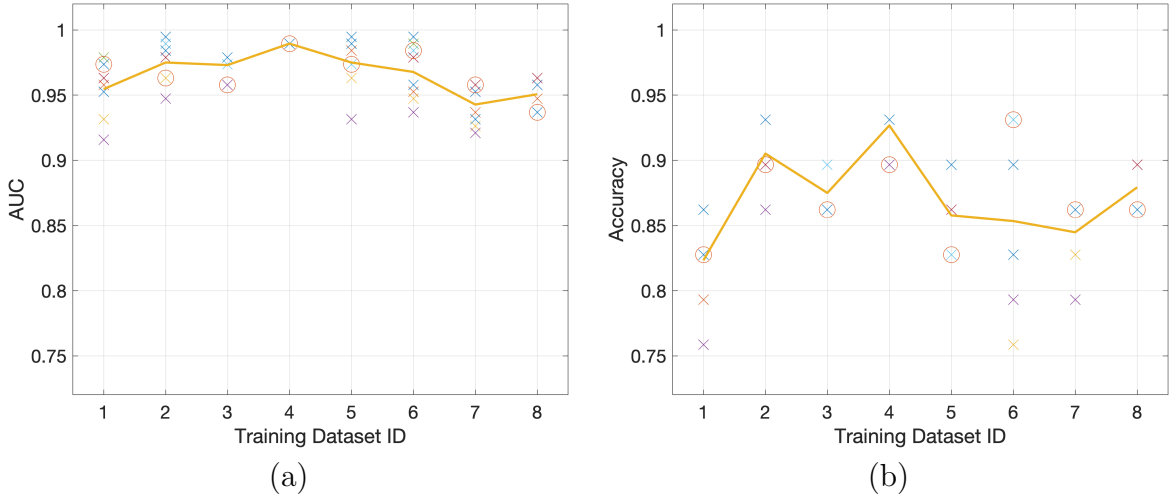


Figure 6: Examine the robustness of CVW when GMM representations of training and test data are generated under different setups. (a) AUC; (b) Classification accuracy. There are 8 datasets each contain GMMs created under a specific setup. Each dataset is used once for training, and for any given training dataset, the test data are taken from the 8 datasets respectively. The horizontal axis shows the training dataset ID, while at each training data set, AUCs or accuracy levels based on the 8 different test datasets are shown. When training and test samples are from the same dataset, the result is shown by a circled cross.

numbers of components and are generated by different clustering schemes. Denote the collections of GMM-S- ζ 's, $\zeta = 3, 5, 7, 10$, respectively by \mathbb{D}_i , $i = 1, \dots, 4$ and the collections of GMM-C- ζ 's, $\zeta = 3, 5, 7, 10$ by \mathbb{D}_i , $i = 5, \dots, 8$. Take \mathbb{D}_1 as an example. In leave-one-out evaluation, we trained our model using GMMs in \mathbb{D}_1 , leaving out one patient. We then applied this model to the left-out patient represented by a GMM from each \mathbb{D}_i , $i = 1, \dots, 8$. So for any given \mathbb{D}_i , we obtained 8 evaluation results, each corresponding to which \mathbb{D}_j the test data come from. The results are shown in Figure 6 (left plot for AUC and right plot for accuracy). For each training data \mathbb{D}_i , we also computed the average performance over all test data \mathbb{D}_j 's (the solid lines in the plots). In addition, when the training \mathbb{D}_i and test \mathbb{D}_j match, that is, $i = j$, we indicate the performance by a circle in the plots. As shown in the figure, the mismatch between the training \mathbb{D}_i and testing \mathbb{D}_j does not cause much difference in performance, especially viewed from an average sense. Sometimes, the mismatched test data even yield slightly better results than the matched test data.

Results summarized in Figure 6 further demonstrate that CVW is robust even when the number of components in GMM differs between training and test sets. Importantly, they also indicate a remarkable advantage of CVW over vector-based classification methods. In order to apply vector-based classification algorithms, the patients in both training and test sets must have the same number of clusters which are also aligned. In contrast, CVW can be applied as long as the patients are represented by GMMs. This flexibility allows us to cluster training and test data independently without restriction on the number of components. As shown by Figure 6, when the setups for creating the GMMs differ between training and test subjects, the influence on classification performance is marginal.

4.4.2 Breast cancer and uveal melanoma data analysis

In this section, we present our analyses of two additional datasets. We first downloaded single-cell data from a total of 26 breast cancer patients, with 16 of them diagnosed as either ER+ (luminal) or HER2+ and the remaining 10 diagnosed as TNBC (triple negative breast cancer) (Wu et al., 2021). Refer to this dataset at BC. In our analysis, TNBC is taken as class 1 and the other two types are class 0. Wu et al. (2021) investigated the cellular heterogeneity of scRNA-seq data obtained from pre-treatment tumors of 26 patients. Their analysis unveiled significant heterogeneity in epithelial, immune, and mesenchymal phenotypes within each tumor. At least nine major cell types were identified, falling into 49 distinct cell subsets at high resolution. In our analysis, we aim to explore whether these diverse cell types can contribute to predicting cancer types in patients.

The second dataset is from the study of uveal melanoma (UM), a highly metastatic cancer largely unresponsive to treatment, including checkpoint immunotherapy. UMs can be further classified into two classes using a widely adopted 15-gene expression profile (GEP) test. Class 1 UMs are associated with a low metastatic risk, while class 2 UMs carry a high risk of metastasis. A recent paper has performed a single-cell analysis of UMs and identified potential discriminative features among tumor cells between class 1 and 2 UMs (Durante et al., 2020). We downloaded the scRNA-seq of tumor cells from 11 tumor samples, 3 in class 1 and the remaining in class 2. Similarly, in this paper, we would like to study whether the scRNA-seq data can contribute to predicting UM classes. For both

datasets, we select the top 100 highly variable genes and derive the GMM for each patient following a similar approach as in the previous example.

We show the performance on BC data in Figure 7(a), (b). The left panel shows AUC and classification accuracy obtained with a varying number of canonical variates, using GMM-S-7’s. The plot shows that the best AUC and accuracy are achieved in the range from 38 to 42, and in terms of both measures, CVW significantly outperforms PMM without dimension reduction. In the right panel, we compare results obtained from SVM, RF, LR, MLP, CVW-C, and CVW-S. Results are shown for GMMs with $\zeta = 3, 5, 7,$ and 10 . The number of canonical variates is set to 40. In the legend on the right hand side, the average AUCs or accuracy levels across ζ for each algorithm are listed with the standard deviation in parenthesis. On average, CVW-C and CVW-S perform similarly with the former slightly better in AUC and the latter slightly better in accuracy; and they both outperform SVM, RF, and LR. MLP achieves the best average AUC, but its accuracy is lower than those obtained by CVW-C and CVW-S. The standard deviation values show that SVM’s results vary most dramatically when ζ changes.

Similarly we show the performance on UM data in Figure 7(c) and (d). The plot on the left is based on GMMs with $\zeta = 7$ obtained by the separate clustering scheme. It shows that when the number of canonical variates is in the range of 13 to 17, AUC is the best, while the accuracy stays at the same level all across. We compare CVW-S and CVW-C with SVM, RF, LR, and MLP in the plot on the right. For CVW-S, we use 13 canonical variates, while for CVW-C, one canonical variate is used. Based on the average performance shown in the legends on the right hand side, CVW-S outperforms all other algorithms by AUC and is only moderately worse than LR by accuracy. In addition, with both CVW-S and CVW-C, the standard deviations are small with different values of ζ . In contrast, SVM, MLP, and LR show significantly high standard deviations in terms of AUC and accuracy.

4.4.3 Evaluation of OTAF with Benchmark Classification Methods

In most of our analyses, we compare OTAF followed by PMM with the benchmark classifiers to examine the potential advantage of performing classification directly in the space of distributions, rather than converting distributions into fixed-length feature vectors for conventional classifiers. Although OTAF is a dimension-reduction approach originally designed to work with distance-based classification methods, it is informative to examine whether OTAF also benefits other types of classifiers. For the three datasets (PF, BC, and UM), we applied OTAF to reduce the data dimension across a range of values using GMMs with $\zeta = 7$ components. Feature extraction (as described in Section 4.2) was then performed on the marginal GMMs in the reduced dimensions. Figure 8 presents the classification performance of SVM, RF, LR, and MLP at different reduced dimensions in terms of AUC and accuracy. For reference, the results obtained in the original dimensions are included in the legend boxes. The findings show that, for each dataset, at certain reduced dimensions, these benchmark methods can achieve improved performance. For example, on the PF dataset, SVM achieves an AUC of 0.842 and an accuracy of 0.724 using the 30-dimensional original data, whereas with the 3-dimensional representation provided by

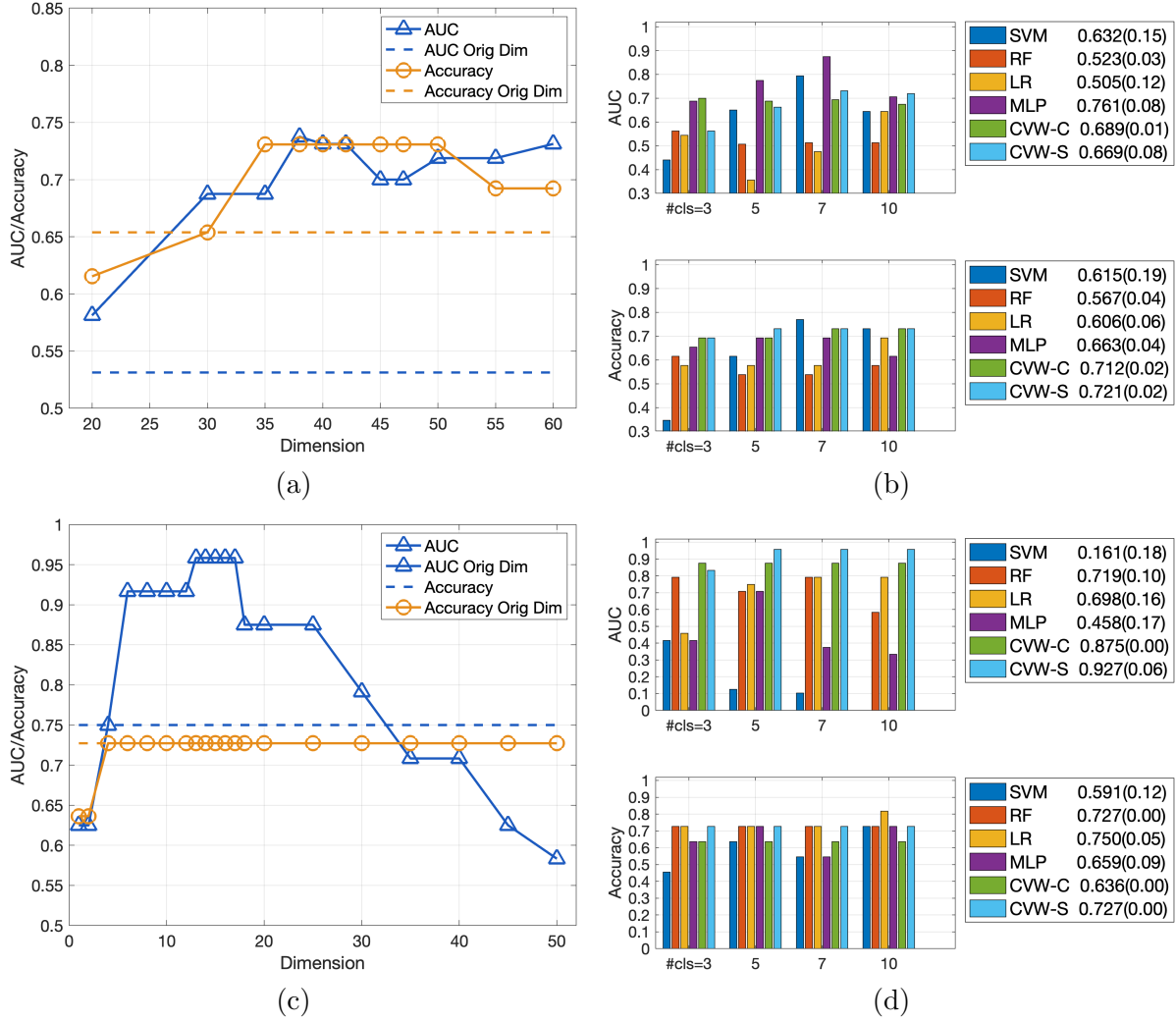
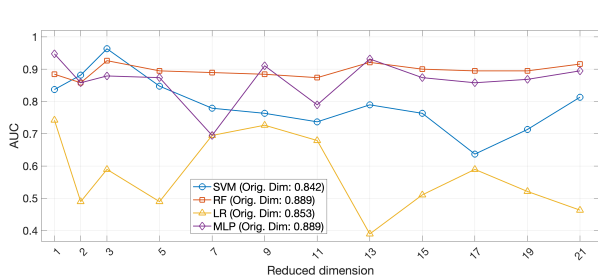
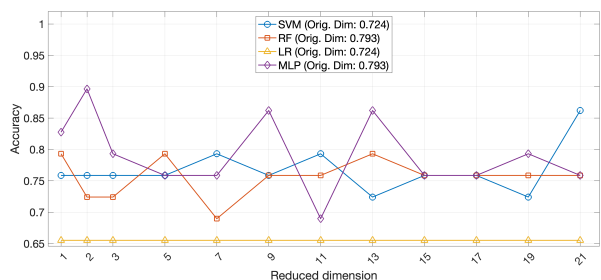


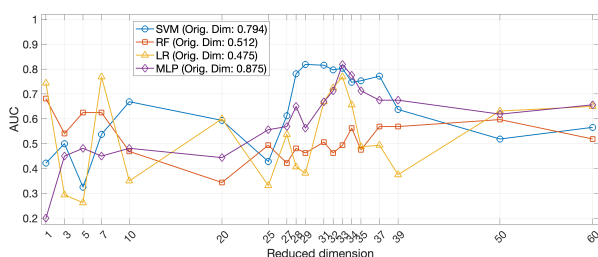
Figure 7: Classification performance on breast cancer (BC) and un.melanoma (UM) data. Top row: BC. Bottom row: UM. (a) and (c): Results across different numbers of canonical variates for GMM-S with $\zeta = 7$; (b) and (d): Compare SVM, RF, LR, MLP, CVW-C, and CVW-S over $\zeta \in \{3, 5, 7, 10\}$. In the legends on the right hand side, average AUCs and accuracy levels across ζ 's with standard deviation are listed.



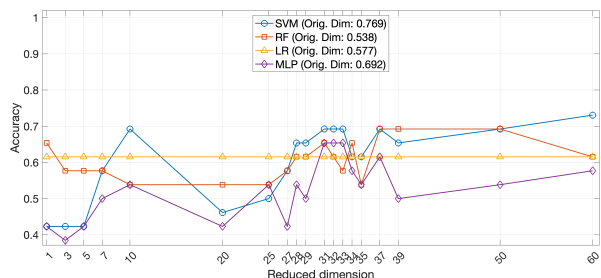
(a) PF: AUC



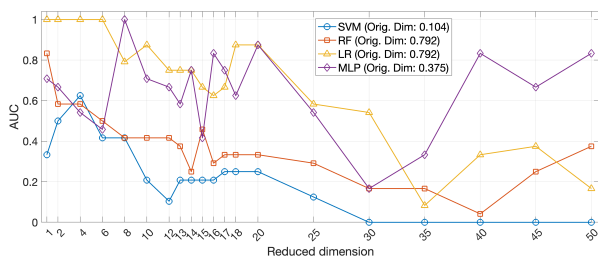
(b) PF: Accuracy



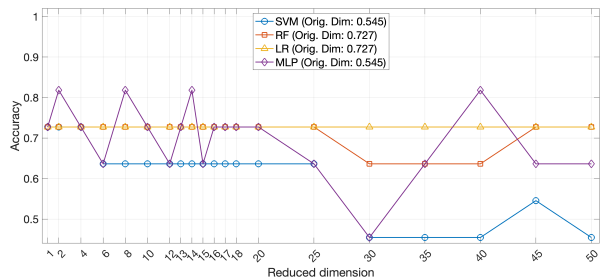
(c) BC: AUC



(d) BC: Accuracy



(e) UM: AUC



(f) UM: Accuracy

Figure 8: Performance of SVM, LR, RF, and MLP on three datasets (PF, BC, UM) after OTAF-based dimension reduction. Left column shows AUC; right column shows classification accuracy. Leave-one-out evaluation is applied. In the legends, AUC or the accuracy obtained with the original dimension is listed as a baseline for comparison. Although OTAF is designed for distance-based classifiers, the dimension-reduced representations often benefit these vector-based classification methods.

OTAF, the AUC exceeds 0.95 and the accuracy rises above 0.75.

4.5 Study of Ascending and Convergence Properties

To study the convergence behavior of the OTAF algorithm, we monitored Fisher’s ratio across iterations and calculated the Grassmann distance between the subspaces identified in consecutive iterations (specifically, comparing iteration τ with iteration $\tau - 1$ starting from $t = 2$). We refer to (Ye and Lim, 2016) for the definition of Grassmann distance. For each dataset, we conducted experiments using GMM-S- ζ , $\zeta = 3, 5, 7, 10$. The results for each ζ value are represented as individual curves in the plots of Figure 9. The plots in Figure 9(a), (b), (c) correspond to orthonormal projections, while those in Figure 9(d), (e), (f) correspond to non-orthonormal projections. For the IP dataset, where dimensionality is reduced to one, there is no distinction between orthonormal and non-orthonormal projections. Therefore, for non-orthonormal projections, we present results only for the BC and UM datasets. In the case of the UM dataset, we offer findings for two different numbers of canonical variates.

Several observations are noted from our study. Regarding Fisher’s ratio, we observe rapid convergence; typically, the ratio stabilizes after just a few iterations. However, an increase in d tends to introduce a minor degree of oscillation. The Grassmann distance suggests that the identified subspace undergoes slight variations. Except for the PF data (reduced to $d = 1$), the Grassmann distance does not converge to zero, indicating continual changes in the subspace structure, possibly oscillation between spaces. When comparing orthonormal with non-orthonormal projections, the latter exhibits a somewhat lower level of oscillation, yet the Grassmann distance remains above zero. Interestingly, we found that orthonormal projections generally yield better classification results.

Given that the objective of identifying canonical variates is to enhance classification rather than serving as the final goal, we investigated how the oscillations depicted in Figure 9 impact classification performance. Focusing on the BC and UM datasets, we analyzed how AUC achieved by the canonical variates varies with the number of iterations. The results, corresponding to the GMM-S- ζ , $\zeta = 3, 5, 7, 10$ are provided in Figure 10. Our observations indicate that the AUC often attains a near-optimal value within just two or three iterations. Beyond this point, while the performance for the BC dataset shows some fluctuation with additional iterations, it generally remains stable for the UM dataset. This suggests that while the number of iterations can influence classification performance, particularly in the case of the BC data, the effect is relatively modest.

5 Conclusions and Discussions

In this paper, we have adapted the principle of Fisher’s ratio to the context of the Wasserstein metric space and formulated the problem of finding canonical variates. We introduce a new algorithm designed to optimize Fisher’s ratio and validate its efficacy using three real-world datasets. Our method uses pairwise distances between instances, a technique that, while offering significant benefits, is computationally intensive due to the necessity of calculating pairwise Wasserstein distances. However, it is worth noting that this process

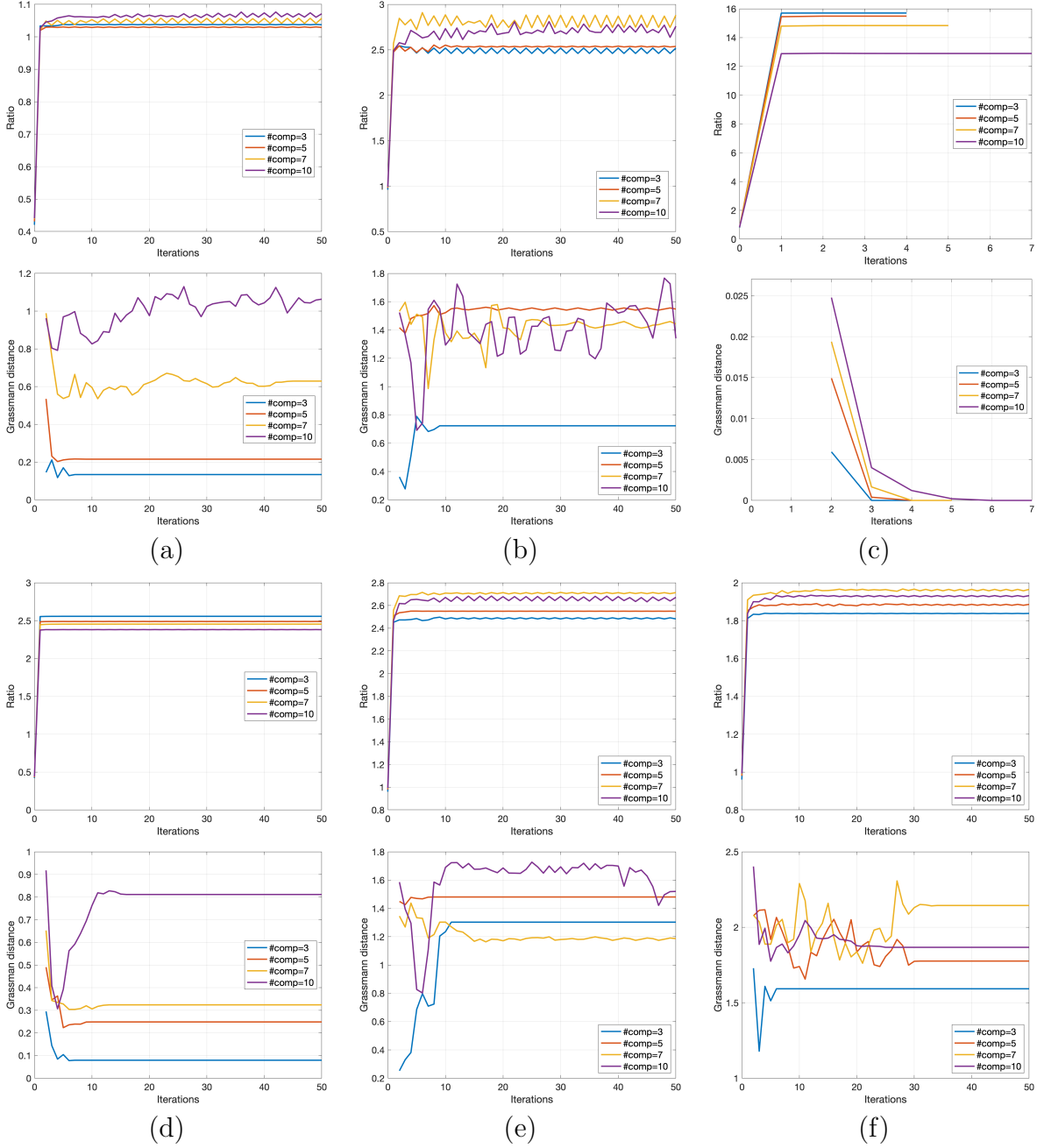


Figure 9: Convergence study based on BC, UM, and PF datasets. For each dataset, the Fisher's ratio of variations and the Grassmann distance between subspaces found in consecutive iterations are shown with respect to the number of iterations. (a)~(c): Orthonormal projection for datasets BC ($d = 40$), UM ($d = 13$), PF ($d = 1$) respectively. (d)~(f): Non-orthonormal project for BC ($d = 40$), UM ($d = 13$), and UM ($d = 25$). Here, d denotes The number of canonical variates.

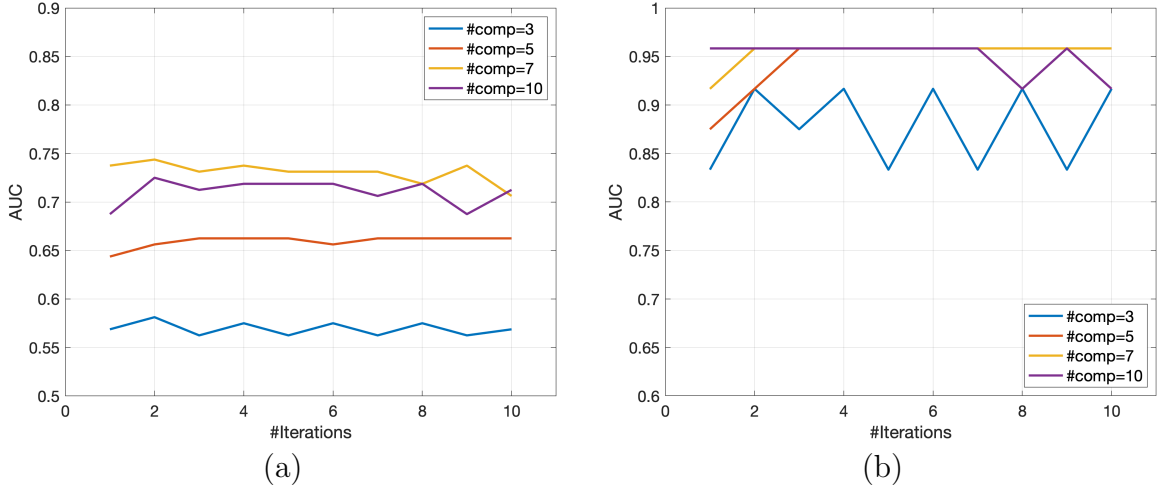


Figure 10: AUC versus the number of iterations. (a) Breast cancer data. (b) Un_melanoma data.

is embarrassingly parallelizable. Importantly, by utilizing pairwise distances, we can easily adjust which instances to consider, thereby focusing on those that are more difficult to classify—a strategy valuable for improving classification performance.

To further reduce the computational load, we can explore alternative strategies, such as selective sampling and traditional methods of assessing within and between-class variations. One such approach involves calculating the Wasserstein barycenters for each class and then evaluating variation based on the cumulative distances between individual instances and their respective class barycenters. Pursuing these methodologies could lead to the development of diverse algorithms, an area we aim to explore in future research.

Acknowledgments

Jia Li’s research is supported by the National Science Foundation under grant no. CCF-2205004. Lin Lin’s research is supported by NCI CCSG P30CA014236 and Duke University Center for AIDS Research (CFAR) AI064518.

A

We prove Eqs. (9) and (10) in Section 3.2. We prove for the case of V_B as the proof for V_W follows likewise. Recall that

$$\bar{V}_B(A, \Pi^*) = \frac{1}{|\mathcal{I}_B|} \sum_{(k_1, k_2) \in \mathcal{I}_B} \sum_{i=1}^{m_{k_1}} \sum_{j=1}^{m_{k_2}} \pi_{i,j}^{(k_1, k_2)} \cdot \left\| A^t \cdot x_i^{(k_1)} - A^t \cdot x_j^{(k_2)} \right\|^2$$

Note that

$$\begin{aligned}
& \left\| A^t \cdot x_i^{(k_1)} - A^t \cdot x_j^{(k_2)} \right\|^2 \\
&= \text{tr} \left[(A^t \cdot x_i^{(k_1)} - A^t \cdot x_j^{(k_2)})^t \cdot (A^t \cdot x_i^{(k_1)} - A^t \cdot x_j^{(k_2)}) \right] \\
&= \text{tr} \left[(A^t \cdot x_i^{(k_1)} - A^t \cdot x_j^{(k_2)}) \cdot (A^t \cdot x_i^{(k_1)} - A^t \cdot x_j^{(k_2)})^t \right] \\
&= \text{tr} \left[A^t (x_i^{(k_1)} - x_j^{(k_2)}) (x_i^{(k_1)} - x_j^{(k_2)})^t \cdot A \right].
\end{aligned}$$

Hence

$$\begin{aligned}
& \sum_{(k_1, k_2) \in \mathcal{I}_B} \sum_{i=1}^{m_{k_1}} \sum_{j=1}^{m_{k_2}} \pi_{i,j}^{(k_1, k_2)} \cdot \left\| A^t \cdot x_i^{(k_1)} - A^t \cdot x_j^{(k_2)} \right\|^2 \\
&= \sum_{(k_1, k_2) \in \mathcal{I}_B} \sum_{i=1}^{m_{k_1}} \sum_{j=1}^{m_{k_2}} \text{tr} \left[A^t \cdot \pi_{i,j}^{(k_1, k_2)} \cdot (x_i^{(k_1)} - x_j^{(k_2)}) (x_i^{(k_1)} - x_j^{(k_2)})^t \cdot A \right] \\
&= \text{tr} \left[A^t \cdot \left(\sum_{(k_1, k_2) \in \mathcal{I}_B} \sum_{i=1}^{m_{k_1}} \sum_{j=1}^{m_{k_2}} \pi_{i,j}^{(k_1, k_2)} \cdot (x_i^{(k_1)} - x_j^{(k_2)}) (x_i^{(k_1)} - x_j^{(k_2)})^t \right) \cdot A \right].
\end{aligned}$$

Since

$$C_B = \frac{1}{|\mathcal{I}_B|} \cdot \sum_{(k_1, k_2) \in \mathcal{I}_B} \sum_{i=1}^{m_{k_1}} \sum_{j=1}^{m_{k_2}} \pi_{i,j}^{(k_1, k_2)} \cdot (x_i^{(k_1)} - x_j^{(k_2)}) (x_i^{(k_1)} - x_j^{(k_2)})^t,$$

we have shown that $\bar{V}_B(A, \Pi^*) = \text{tr}(A^t C_B A)$. The proof for $\bar{V}_W(A, \Pi^*) = \text{tr}(A^t C_W A)$ is similar and skipped here.

B

We prove Eqs. (13) and (14) in Section 3.3. Recall that $\hat{\pi}$ is the joint distribution of independent random vectors Z_1 and Z_2 in \mathbb{R}^d with marginal distributions $\phi_1 \sim N(\mu_1, \Sigma_1)$ and $\phi_2 \sim N(\mu_2, \Sigma_2)$.

$$\begin{aligned}
& \widehat{W}^2(\phi_1, \phi_2) = E_{\hat{\pi}} \|Z_1 - Z_2\|^2 \\
&= E (Z_1 - Z_2)^t (Z_1 - Z_2) \\
&= E [Z_1 - \mu_1 - (Z_2 - \mu_2) + \mu_1 - \mu_2]^t [Z_1 - \mu_1 - (Z_2 - \mu_2) + \mu_1 - \mu_2] \\
&= E (Z_1 - \mu_1)^t (Z_1 - \mu_1) + E (Z_2 - \mu_2)^t (Z_2 - \mu_2) \\
&\quad - 2E (Z_1 - \mu_1) (Z_2 - \mu_2) + \|\mu_1 - \mu_2\|^2 \\
&= E (Z_1 - \mu_1)^t (Z_1 - \mu_1) + E (Z_2 - \mu_2)^t (Z_2 - \mu_2) + \|\mu_1 - \mu_2\|^2.
\end{aligned}$$

The last equality follows from the independence of Z_1 and Z_2 . Also note that

$$(Z_1 - \mu_1)^t (Z_1 - \mu_1) = \text{tr}[(Z_1 - \mu_1)^t (Z_1 - \mu_1)] = \text{tr}[(Z_1 - \mu_1)(Z_1 - \mu_1)^t]$$

Hence

$$\begin{aligned} E(Z_1 - \mu_1)^t(Z_1 - \mu_1) &= E[\text{tr}((Z_1 - \mu_1)(Z_1 - \mu_1)^t)] \\ &= \text{tr}[E((Z_1 - \mu_1)(Z_1 - \mu_1)^t)] = \text{tr}(\Sigma_1) . \end{aligned}$$

Similarly, we have $E(Z_2 - \mu_2)^t(Z_2 - \mu_2) = \text{tr}(\Sigma_2)$. We thus have shown that

$$\widehat{W}^2(\phi_1, \phi_2) = \|\mu_1 - \mu_2\|^2 + \text{tr}[\Sigma_1 + \Sigma_2] .$$

Since $\|\mu_1 - \mu_2\|^2 = \text{tr}((\mu_1 - \mu_2) \cdot (\mu_1 - \mu_2)^t)$, we also have

$$\widehat{W}^2(\phi_1, \phi_2) = \text{tr}[\Sigma_1 + \Sigma_2 + (\mu_1 - \mu_2) \cdot (\mu_1 - \mu_2)^t] .$$

Since $P(\phi_i, A) \sim N(A^t \mu_i, A^t \Sigma_i A)$, $i = 1, 2$,

$$\begin{aligned} \widehat{W}^2(P(\phi_1, A), P(\phi_2, A)) &= \text{tr}[A^t \Sigma_1 A + A^t \Sigma_2 A + A^t (\mu_1 - \mu_2) \cdot (\mu_1 - \mu_2)^t A] \\ &= \text{tr}[A^t \cdot (\Sigma_1 + \Sigma_2 + (\mu_1 - \mu_2) \cdot (\mu_1 - \mu_2)^t) \cdot A] . \end{aligned}$$

C

We prove Eqs. (17) and (18) in Section 3.3. We prove for the case of $\widehat{V}_B(A, \Pi^*)$. The proof for $\widehat{V}_W(A, \Pi^*)$ is similar and skipped. By Eqs. (13) and (14) ,

$$\widehat{W}^2(P(\phi_1, A), P(\phi_2, A)) = \text{tr}[A^t \cdot (\Sigma_1 + \Sigma_2 + (\mu_1 - \mu_2) \cdot (\mu_1 - \mu_2)^t) \cdot A] . \quad (22)$$

Substitute Eq. (22) in the following:

$$\widehat{V}_B(A, \Pi^*) = \frac{1}{|\mathcal{I}_B|} \sum_{(k_1, k_2) \in \mathcal{I}_B} \sum_{i=1}^{m_{k_1}} \sum_{j=1}^{m_{k_2}} \pi_{i,j}^{(k_1, k_2)} \cdot \widehat{W}^2(P(\phi_i^{(k_1)}, A), P(\phi_j^{(k_2)}, A))$$

and apply the additive property of trace, we get

$$\widehat{V}_B(A, \Pi^*) = \text{tr}[A^t \hat{C}_B A] ,$$

where

$$\hat{C}_B = \frac{1}{|\mathcal{I}_B|} \sum_{(k_1, k_2) \in \mathcal{I}_B} \sum_{i=1}^{m_{k_1}} \sum_{j=1}^{m_{k_2}} \pi_{i,j}^{(k_1, k_2)} \cdot \left[\Sigma_i^{(k_1)} + \Sigma_j^{(k_2)} + (\mu_i^{(k_1)} - \mu_j^{(k_2)}) \cdot (\mu_i^{(k_1)} - \mu_j^{(k_2)})^t \right] .$$

Note that

$$\sum_{i=1}^{m_{k_1}} \sum_{j=1}^{m_{k_2}} \pi_{i,j}^{(k_1, k_2)} \cdot \Sigma_i^{(k_1)} = \sum_{i=1}^{m_{k_1}} \Sigma_i^{(k_1)} \sum_{j=1}^{m_{k_2}} \pi_{i,j}^{(k_1, k_2)} = \sum_{i=1}^{m_{k_1}} p_i^{(k_1)} \Sigma_i^{(k_1)} ,$$

and, similarly, $\sum_{i=1}^{m_{k_1}} \sum_{j=1}^{m_{k_2}} \pi_{i,j}^{(k_1,k_2)} \cdot \Sigma_j^{(k_2)} = \sum_{j=1}^{m_{k_2}} p_j^{(k_2)} \Sigma_j^{(k_2)}$. Thus we have shown Eq. (15):

$$\begin{aligned} \hat{C}_B &= \frac{1}{|\mathcal{I}_B|} \sum_{(k_1,k_2) \in \mathcal{I}_B} \sum_{i=1}^{m_{k_1}} \sum_{j=1}^{m_{k_2}} \pi_{i,j}^{(k_1,k_2)} (\mu_i^{(k_1)} - \mu_j^{(k_2)}) \cdot (\mu_i^{(k_1)} - \mu_j^{(k_2)})^t \\ &\quad + \frac{1}{|\mathcal{I}_B|} \sum_{(k_1,k_2) \in \mathcal{I}_B} \left[\sum_{i=1}^{m_{k_1}} p_i^{(k_1)} \Sigma_i^{(k_1)} + \sum_{j=1}^{m_{k_2}} p_j^{(k_2)} \Sigma_j^{(k_2)} \right]. \end{aligned}$$

D

We prove Theorem 1 in Section 3.4. Let $r(a) = r(a, \Pi^*)$ be the Fisher's ratio objective function, where Π^* is the optimal transport coupling associated with the projection a . Let OTAF denote the iterative optimization procedure composed of the A-step (maximization over a) and the OT-step (optimal coupling update Π).

Condition C1 (Required for monotonicity): Assume that for any projection direction a , the optimal coupling Π^* satisfies the non-decreasing ratio condition relative to any non-optimal coupling Π : $r(a) \geq r(a, \Pi)$

Statement: If Condition C1 holds, the OTAF algorithm generates a sequence of objective values $\{r(a_\tau)\}_{\tau \geq 1}$ that is non-decreasing and bounded above, guaranteeing convergence to a set of stationary points. Furthermore, if (a_τ, Π_τ) is not a stationary point of the objective $r(a)$, then the iteration guarantees a strictly ascending step, $r(a_{\tau+1}) - r(a_\tau) > 0$.

Proof: We first justify condition C1. Since the objective is $r(a, \Pi) = \frac{\bar{V}_B(a, \Pi)}{\bar{V}_W(a, \Pi)}$, the inequality $r(a) \stackrel{\text{Def}}{=} r(a, \Pi^*) \geq r(a, \Pi)$ is true if the optimal coupling Π^* reduces the within-class variable (\bar{V}_W) relatively more than it reduces the between-class variation (\bar{V}_B). Thus, Condition C1 holds when the projection a yields a strong discriminant direction. In this case: (1) \bar{V}_W reduction is larger as OT excels at finding the lowest cost (distance) between similar distributions (within-class), leading to a significant relative reduction of \bar{V}_W . (2) \bar{V}_B reduction is modest as for well-separated distributions (between-class), the optimal coupling still reduces the cost, but the reduction is relatively less pronounced than for the within-class distributions. Thus, when the relative decrease in the denominator (\bar{V}_W) is greater than the relative decrease in the numerator (\bar{V}_B), the ratio increases, and Condition C1 is satisfied.

Next, we show that the objective value is non-decreasing in every iteration, $r(a_{\tau+1}) \geq r(a_\tau)$. The iteration consists of two consecutive steps linked by the following inequalities:

$$r(a_{\tau+1}) \stackrel{\text{C1}}{\geq} r(a_{\tau+1}, \Pi_\tau) \stackrel{\text{A-step}}{\geq} r(a_\tau, \Pi_\tau) \stackrel{\text{Def}}{=} r(a_\tau).$$

Step 1. OT-Step ($r(a_{\tau+1}) \geq r(a_{\tau+1}, \Pi_\tau)$) Since $\Pi_{\tau+1}$ is the optional coupling (Π^*) for the projection $a_{\tau+1}$, by Condition C1, we have $r(a_{\tau+1}) = r(a_{\tau+1}, \Pi_{\tau+1}) \geq r(a_{\tau+1}, \Pi_\tau)$.

Step 2. A-Step ($r(a_{\tau+1}, \Pi_\tau) \geq r(a_\tau, \Pi_\tau)$) The A-step is a maximization of the function $r(\cdot, \Pi_\tau)$ over a . Since $a_{\tau+1}$ is the maximizer and a_τ is a feasible point: $r(a_{\tau+1}, \Pi_\tau) \geq r(a_\tau, \Pi_\tau)$.

Combining the above two steps, and using the definition $r(a_\tau) = r(a_\tau, \Pi_\tau)$, we establish the non-decreasing property: $r(a_{\tau+1}) \geq r(a_{\tau+1}, \Pi_\tau) \geq r(a_\tau)$. Since $r(a)$ is a ratio of variances, it is bounded above. A non-decreasing, bounded sequence is guaranteed to converge to a limit value.

For the strictly ascending property, assume the current iteration a_τ is not a stationary point. By the maximization property of the A-step, the resulting objective value must be strictly greater than the initial value:

$$\exists \delta_\tau^A > 0 \quad \text{such that} \quad r(a_{\tau+1}, \Pi_\tau) = r(a_\tau, \Pi_\tau) + \delta_\tau^A.$$

Then the difference

$$r(a_{\tau+1}) - r(a_\tau) = r(a_{\tau+1}, \Pi_{\tau+1}) - r(a_\tau, \Pi_\tau)$$

can be decomposed by:

$$r(a_{\tau+1}) - r(a_\tau) = \underbrace{[r(a_{\tau+1}, \Pi_{\tau+1}) - r(a_{\tau+1}, \Pi_\tau)]}_{\text{Change from OT-step } (\Delta_{\text{OT}})} + \underbrace{[r(a_{\tau+1}, \Pi_\tau) - r(a_\tau, \Pi_\tau)]}_{\text{Change from A-step } (\Delta_{\text{A}})}$$

From Condition C1, the OT-step change is non-negative:

$$\Delta_{\text{OT}} = r(a_{\tau+1}, \Pi_{\tau+1}) - r(a_{\tau+1}, \Pi_\tau) \geq 0$$

From the non-stationary condition, the A-step change is strictly positive:

$$\Delta_{\text{A}} = r(a_{\tau+1}, \Pi_\tau) - r(a_\tau, \Pi_\tau) = \delta_\tau^A > 0$$

Therefore, the total objective increase μ_τ is strictly positive:

$$\mu_\tau = \Delta_{\text{OT}} + \Delta_{\text{A}} \geq 0 + \delta_\tau^A > 0$$

Since $r(a_\tau)$ is strictly ascending at every non-stationary point, the sequence $\{r(a_\tau)\}$ cannot oscillate or remain trapped at a non-stationary fixed point. Combined with the bounded nature of the objective, the algorithm must converge to a set of stationary points.

References

Ager, C. R., Zhang, M., Chaimowitz, M., Bansal, S., Tagore, S., Obradovic, A., Jugler, C., Rogava, M., Melms, J. C., McCann, P., Spina, C., Drake, C. G., Dallos, M. C., and Izar, B. (2023). Klr1 marks tumor-infiltrating cd4 t cell subsets associated with tumor progression and immunotherapy response. *Journal for ImmunoTherapy of Cancer*, 11(9):e006782.

- Aid, M., Colarusso, A., Walker-Sperling, V., and Barouch, D. H. (2023). Peripheral blood biomarkers predict viral rebound following antiretroviral therapy discontinuation in siv-infected, early art-treated rhesus macaques. *Cell Reports Medicine*, 4(7).
- Aleman, A., Upadhyaya, B., Tuballes, K., Kappes, K., Gleason, C., Beach, K., Agte, S., Srivastava, K., Andre, D., Azad, A., Banu, R., Bermúdez-González, M. C., Cai, G., Cognigni, C., David, K., Floda, D., Firpo, A., Kleiner, G., Lyttle, N., Mendez, W., Mulder, L. C. F., Mendu, R., Oostenink, A., Rooker, A., Russo, K., Salimbangon, A., Saksena, M., Shin, A., Sominsky, L., Van Oekelen, O., Barcessat, V., Bhardwaj, N., Kim-Schulze, S., Gnjjatic, S., Brown, B., Cordon-Cardo, C., Krammer, F., Merad, M., Jagannath, S., Wajnberg, A., Simon, V., and Parekh, S. (2021). Variable cellular responses to SARS-CoV-2 in fully vaccinated patients with multiple myeloma. *Cancer Cell*, 39(11):1442–1444.
- Anwar, I. J., DeLaura, I., Ladowski, J. M., Schilirò, D., Gao, Q., Manook, M., Yoon, J., Belloni, R., Park, A., Schuster, D. J., Song, M., Lin, L., Farris, A. B., Magnani, D., Williams, K., Kwun, J., and Knechtle, S. J. (2025). Cd154 blockade effectively controls antibody-mediated rejection in highly sensitized nonhuman primate kidney transplant recipients. *Science Translational Medicine*, 17(779):eadn8130.
- Benamou, J.-D., Carlier, G., Cuturi, M., Nenna, L., and Peyré, G. (2015). Iterative Bregman projections for regularized transportation problems. *SIAM J. Sci. Comp. (SISC)*, 37(2):A1111–A1138.
- Bonneel, N., Rabin, J., Peyré, G., and Pfister, H. (2015). Sliced and radon wasserstein barycenters of measures. *Journal of Mathematical Imaging and Vision*, 51:22–45.
- Brummelman, J., Haftmann, C., Núñez, N. G., Alvisi, G., Mazza, E. M. C., Becher, B., and Lugli, E. (2019). Development, application and computational analysis of high-dimensional fluorescent antibody panels for single-cell flow cytometry. *Nature Protocols*, 14(7):1946–1969.
- Chen, Y., Ye, J., and Li, J. (2019). Aggregated Wasserstein distance and state registration for hidden Markov models. *IEEE transactions on pattern analysis and machine intelligence*, 42(9):2133–2147.
- Cron, A., Gouttefangeas, C., Frelinger, J., Lin, L., Singh, S. K., Britten, C. M., Welters, M. J. P., van der Burg, S. H., West, M., and Chan, C. (2013). Hierarchical modeling for rare event detection and cell subset alignment across flow cytometry samples. *PLOS Computational Biology*, 9(7):1–14.
- Cui, H., Wang, C., Maan, H., Pang, K., Luo, F., Duan, N., and Wang, B. (2024). scgpt: toward building a foundation model for single-cell multi-omics using generative ai. *Nature Methods*, 21(8):1470–1480.
- Cuturi, M. (2013). Sinkhorn distances: Lightspeed computation of optimal transport. In Burges, C., Bottou, L., Welling, M., Ghahramani, Z., and Weinberger, K., editors, *Advances in Neural Information Processing Systems*, volume 26. Curran Associates, Inc.

- Delon, J. and Desolneux, A. (2020). A Wasserstein-type distance in the space of Gaussian mixture models. *SIAM Journal on Imaging Sciences*, 13(2):936–970.
- Delon, J., Desolneux, A., Facq, L., and Leclaire, A. (2023). Optimal transport between GMM for multiscale texture synthesis. In *International Conference on Scale Space and Variational Methods in Computer Vision (SSVM)*. Springer.
- Delon, J., Desolneux, A., and Salmona, A. (2022). Gromov–Wasserstein distances between Gaussian distributions. *Journal of Applied Probability*, 59(4):1178–1198.
- Deshpande, I., Hu, Y.-T., Sun, R., Pyrros, A., Siddiqui, N., Koyejo, S., Zhao, Z., Forsyth, D., and Schwing, A. G. (2019). Max-sliced wasserstein distance and its use for gans. In *Proceedings of the IEEE/CVF conference on computer vision and pattern recognition*, pages 10648–10656.
- Durante, M. A., Rodriguez, D. A., Kurtenbach, S., Kuznetsov, J. N., Sanchez, M. I., Decatur, C. L., Snyder, H., Feun, L. G., Livingstone, A. S., and Harbour, J. W. (2020). Single-cell analysis reveals new evolutionary complexity in uveal melanoma. *Nature Communications*, 11(1):496.
- Dyikanov, D., Zaitsev, A., Vasileva, T., Wang, I., Sokolov, A. A., Bolshakov, E. S., Frank, A., Turova, P., Golubeva, O., Gantseva, A., Kamysheva, A., Shpudeiko, P., Krauz, I., Abdou, M., Chasse, M., Conroy, T., Merriam, N. R., Alesse, J. E., English, N., Shpak, B., Shchetsova, A., Tikhonov, E., Filatov, I., Radko, A., Bolshakova, A., Kachalova, A., Lugovykh, N., Bulahov, A., Kilina, A., Asanbekov, S., Zheleznyak, I., Skoptsov, P., Alekseeva, E., Johnson, J. M., Curry, J. M., Linnenbach, A. J., South, A. P., Yang, E., Morozov, K., Terenteva, A., Nigmatullina, L., Fastovetz, D., Bobe, A., Balabanian, L., Nomie, K., Yong, S. T., Davitt, C. J., Ryabykh, A., Kudryashova, O., Tazearslan, C., Bagaev, A., Fowler, N., Luginbuhl, A. J., Ataullakhanov, R. I., and Goldberg, M. F. (2024). Comprehensive peripheral blood immunoprofiling reveals five immunotypes with immunotherapy response characteristics in patients with cancer. *Cancer Cell*, 42(5):759–779.e12.
- Flamary, R., Cuturi, M., Courty, N., and Rakotomamonjy, A. (2018). Wasserstein discriminant analysis. *Machine Learning*, 107:1923–1945.
- Furman, D., Jovic, V., Kidd, B., Shen-Orr, S., Price, J., Jarrell, J., Tse, T., Huang, H., Lund, P., Maecker, H. T., Utz, P. J., Dekker, C. L., Koller, D., and Davis, M. M. (2013). Apoptosis and other immune biomarkers predict influenza vaccine responsiveness. *Molecular Systems Biology*, 9(1):659.
- Gray, G. E., Huang, Y., Grunenberg, N., Laher, F., Roux, S., Andersen-Nissen, E., Rosa, S. C. D., Flach, B., Randhawa, A. K., Jensen, R., Swann, E. M., Bekker, L.-G., Innes, C., Lazarus, E., Morris, L., Mkhize, N. N., Ferrari, G., Montefiori, D. C., Shen, X., Sawant, S., Yates, N., Hural, J., Isaacs, A., Phogat, S., DiazGranados, C. A., Lee, C., Sinangil, F., Michael, N. L., Robb, M. L., Kublin, J. G., Gilbert, P. B., McElrath, M. J.,

- Tomaras, G. D., and Corey, L. (2019). Immune correlates of the thai rv144 hiv vaccine regimen in south africa. *Science Translational Medicine*, 11(510):eaax1880.
- Habermann, A. C., Gutierrez, A. J., Bui, L. T., Yahn, S. L., Winters, N. I., Calvi, C. L., Peter, L., Chung, M.-I., Taylor, C. J., Jetter, C., Raju, L., Roberson, J., Ding, G., Wood, L., Sucre, J. M. S., Richmond, B. W., Serezani, A. P., McDonnell, W. J., Mallal, S. B., Bacchetta, M. J., Loyd, J. E., Shaver, C. M., Ware, L. B., Bremner, R., Walia, R., Blackwell, T. S., Banovich, N. E., and Kropski, J. A. (2020). Single-cell RNA sequencing reveals profibrotic roles of distinct epithelial and mesenchymal lineages in pulmonary fibrosis. *Science Advances*, 6(28):eaba1972.
- Hastie, T., Tibshirani, R., Friedman, J. H., and Friedman, J. H. (2009). *The elements of statistical learning: data mining, inference, and prediction*, volume 2. Springer.
- Huizing, G.-J., Peyré, G., and Cantini, L. (2022). Optimal transport improves cell–cell similarity inference in single-cell omics data. *Bioinformatics*, 38(8):2169–2177.
- Johansen, N. and Quon, G. (2019). scalign: a tool for alignment, integration, and rare cell identification from scrna-seq data. *Genome Biology*, 20(1):166.
- Joodaki, M., Shaigan, M., Parra, V., Bülow, R. D., Kuppe, C., Hölscher, D. L., Cheng, M., Nagai, J. S., Goedertier, M., Bouteldja, N., Tesar, V., Barratt, J., Roberts, I. S., Coppo, R., Kramann, R., Boor, P., and Costa, I. G. (2024). Detection of patient-level distances from single cell genomics and pathomics data with optimal transport (pilot). *Molecular Systems Biology*, 20(2):57–74.
- Kolouri, S., Nadjahi, K., Simsekli, U., Badeau, R., and Rohde, G. (2019). Generalized sliced wasserstein distances. *Advances in neural information processing systems*, 32.
- Li, J. and Lin, L. (2021). Optimal transport with relaxed marginal constraints. *IEEE Access*, 9:58142–58160.
- Lin, L., Finak, G., Ushey, K., Seshadri, C., Hawn, T. R., Frahm, N., Scriba, T. J., Mahomed, H., Hanekom, W., Bart, P.-A., Pantaleo, G., Tomaras, G. D., Rerks-Ngarm, S., Kaewkungwal, J., Nitayaphan, S., Pitisuttithum, P., Michael, N. L., Kim, J. H., Robb, M. L., O’Connell, R. J., Karasavvas, N., Gilbert, P., C De Rosa, S., McElrath, M. J., and Gottardo, R. (2015). COMPASS identifies T-cell subsets correlated with clinical outcomes. *Nature Biotechnology*, 33(6):610–616.
- Lin, L., Shi, W., Ye, J., and Li, J. (2023). Multisource single-cell data integration by MAW barycenter for Gaussian mixture models. *Biometrics*, 79(2):866–877.
- Lingblom, C. M. D., Kowli, S., Swaminathan, N., Maecker, H. T., and Lambert, S. L. (2018). Baseline immune profile by CyTOF can predict response to an investigational adjuvanted vaccine in elderly adults. *Journal of Translational Medicine*, 16(1):153.
- Mémoli, F. (2011). Gromov–Wasserstein distances and the metric approach to object matching. *Foundations of computational mathematics*, 11:417–487.

- Mettu, N. B., Waechter, B., Zemla, T. J., Liu, Y., Brady, J. C., Lin, L., Gnjatic, S., Weinhold, K. J., Bekaii-Saab, T. S., Ou, F.-S., and Nixon, A. B. (2023). Correlation of single-cell cytokine secretion with clinical outcome in patients (pts) with metastatic colorectal cancer (mCRC) treated with capecitabine (c), bevacizumab (b), \pm atezolizumab (a). *Journal of Clinical Oncology*, 41(16_suppl):3533–3533.
- Nguyen, B., Rubbens, P., Kerckhof, F.-M., Boon, N., De Baets, B., and Waegeman, W. (2019). Learning single-cell distances from cytometry data. *Cytometry Part A*, 95(7):782–791.
- Paty, F.-P. and Cuturi, M. (2019). Subspace robust wasserstein distances. In *International conference on machine learning*, pages 5072–5081. PMLR.
- Pele, O. and Werman, M. (2009). Fast and robust Earth Mover’s Distances. In *2009 IEEE 12th International Conference on Computer Vision*, pages 460–467.
- Qiao, M. and Li, J. (2016). Distance-based mixture modeling for classification via hypothetical local mapping. *Statistical Analysis and Data Mining: The ASA Data Science Journal*, 9(1):43–57.
- Rubio, A. M., Everaert, C., Damme, E. V., Preter, K. D., and Vermaelen, K. (2023). Circulating immune cell dynamics as outcome predictors for immunotherapy in non-small cell lung cancer. *Journal for ImmunoTherapy of Cancer*, 11(8).
- Seshadri, C., Lin, L., Scriba, T. J., Peterson, G., Freidrich, D., Frahm, N., DeRosa, S. C., Moody, D. B., Prandi, J., Gilleron, M., Mahomed, H., Jiang, W., Finak, G., Hanekom, W. A., Gottardo, R., McElrath, M. J., and Hawn, T. R. (2015). T cell responses against mycobacterial lipids and proteins are poorly correlated in south african adolescents. *The Journal of Immunology*, 195(10):4595–4603.
- Shah, J. A., Musvosvi, M., Shey, M., Horne, D. J., Wells, R. D., Peterson, G. J., Cox, J. S., Daya, M., Hoal, E. G., Lin, L., Gottardo, R., Hanekom, W. A., Scriba, T. J., Hatherill, M., and Hawn, T. R. (2017). A functional toll-interacting protein variant is associated with bacillus calmette-guérin-specific immune responses and tuberculosis. *American Journal of Respiratory and Critical Care Medicine*, 196(4):502–511.
- Stefanski, A.-L., Rincon-Arevalo, H., Schrezenmeier, E., Karberg, K., Szelinski, F., Ritter, J., Chen, Y., Jahrsdörfer, B., Ludwig, C., Schrezenmeier, H., Lino, A. C., and Dörner, T. (2022). B cell characteristics at baseline predict vaccination response in RTX treated patients. *Frontiers in Immunology*, 13.
- Sun, L., Yang, Q., Zhang, J., Guo, W., and Lin, L. (2025). eSPred: Explainable scRNA-seq prediction via customized foundation models and pathway-aware fine-tuning. *bioRxiv*.
- Tanguy, E., Flamary, R., and Delon, J. (2023). Properties of discrete sliced Wasserstein losses. *arXiv preprint arXiv:2307.10352*.
- Villani, C. (2003). *Topics in Optimal Transportation*. American Mathematical Soc.

- Wang, J., Wang, P., and Shafto, P. (2023). Efficient discretization of optimal transport. *Entropy*, 25(6).
- Wang, Z., Zhan, Q., Yang, S., Mu, S., Chen, J., Garai, S., Orzechowski, P., Wagenaar, J., and Shen, L. (2025). Qot: Quantized optimal transport for sample-level distance matrix in single-cell omics. *Briefings in Bioinformatics*, 26(1):bbae713.
- Wu, S. Z., Al-Eryani, G., Roden, D. L., Junankar, S., Harvey, K., Andersson, A., Thennavan, A., Wang, C., Torpy, J. R., Bartonicek, N., Wang, T., Larsson, L., Kaczorowski, D., Weisenfeld, N. I., Uytingco, C. R., Chew, J. G., Bent, Z. W., Chan, C.-L., Gnanasambandapillai, V., Dutertre, C.-A., Gluch, L., Hui, M. N., Beith, J., Parker, A., Robbins, E., Segara, D., Cooper, C., Mak, C., Chan, B., Warriar, S., Ginhoux, F., Millar, E., Powell, J. E., Williams, S. R., Liu, X. S., O’Toole, S., Lim, E., Lundeberg, J., Perou, C. M., and Swarbrick, A. (2021). A single-cell and spatially resolved atlas of human breast cancers. *Nature Genetics*, 53(9):1334–1347.
- Yang, L., Li, J., Sun, D., and Toh, K.-C. (2021). A fast globally linearly convergent algorithm for the computation of wasserstein barycenters. *Journal of Machine Learning Research*, 22(21):1–37.
- Ye, J., Wu, P., Wang, J. Z., and Li, J. (2017). Fast discrete distribution clustering using wasserstein barycenter with sparse support. *IEEE Transactions on Signal Processing*, 65(9):2317–2332.
- Ye, K. and Lim, L.-H. (2016). Schubert varieties and distances between subspaces of different dimensions. *SIAM Journal on Matrix Analysis and Applications*, 37(3):1176–1197.
- Yi, H. and Stanley, N. (2022). Cytoemd: detecting and visualizing between-sample variation in relation to phenotype with earth mover’s distance. In *Proceedings of the 13th ACM International Conference on Bioinformatics, Computational Biology and Health Informatics*, BCB ’22, New York, NY, USA. Association for Computing Machinery.
- Zhang, J., Li, J., and Lin, L. (2023a). Statistical and machine learning methods for immunoprofiling based on single-cell data. *Human Vaccines & Immunotherapeutics*, page 2234792.
- Zhang, J., Sun, L., Ready, N. E., Guo, W., and Lin, L. (2025). cytogpnet: Enhancing clinical outcome prediction accuracy using longitudinal cytometry data in small cohort studies. *Patterns*.
- Zhang, L., Lin, L., and Li, J. (2020). Cps analysis: self-contained validation of biomedical data clustering. *Bioinformatics*, 36(11):3516–3521.
- Zhang, L., Lin, L., and Li, J. (2023b). Multi-view clustering by cps-merge analysis with application to multimodal single-cell data. *PLOS Computational Biology*, 19(4):1–21.

Zhang, M. and Guo, F. R. (2022). BSDE: barycenter single-cell differential expression for case-control studies. *Bioinformatics*, 38(10):2765–2772.

Zou, X., Liu, Y., Wang, M., Zou, J., Shi, Y., Su, X., Xu, J., Tong, H. H., Ji, Y., Gui, L., and Hao, J. (2023). scure identifies cell types responding to immunotherapy and enables outcome prediction. *Cell Reports Methods*, 3(11):100643.